



This is a repository copy of *Recreating silk's fibrillar nanostructure by spinning solubilized, undegummed silk*.

White Rose Research Online URL for this paper:

<https://eprints.whiterose.ac.uk/222705/>

Version: Accepted Version

Article:

Zaki, M. orcid.org/0009-0003-8050-5390, Rajkhowa, R. orcid.org/0000-0002-6811-9126, Holland, C. orcid.org/0000-0003-0913-2221 et al. (5 more authors) (2025) Recreating silk's fibrillar nanostructure by spinning solubilized, undegummed silk. *Advanced Materials*. e2413786. ISSN 0935-9648

<https://doi.org/10.1002/adma.202413786>

© 2025 The Authors. Except as otherwise noted, this author-accepted version of a journal article published in *Advanced Materials* is made available via the University of Sheffield Research Publications and Copyright Policy under the terms of the Creative Commons Attribution 4.0 International License (CC-BY 4.0), which permits unrestricted use, distribution and reproduction in any medium, provided the original work is properly cited. To view a copy of this licence, visit <http://creativecommons.org/licenses/by/4.0/>

Reuse

This article is distributed under the terms of the Creative Commons Attribution (CC BY) licence. This licence allows you to distribute, remix, tweak, and build upon the work, even commercially, as long as you credit the authors for the original work. More information and the full terms of the licence here:

<https://creativecommons.org/licenses/>

Takedown

If you consider content in White Rose Research Online to be in breach of UK law, please notify us by emailing eprints@whiterose.ac.uk including the URL of the record and the reason for the withdrawal request.



eprints@whiterose.ac.uk
<https://eprints.whiterose.ac.uk/>

Recreating Silk's Fibrillar Nanostructure by Spinning Solubilized, Undegummed Silk

*Martin Zaki, Rangam Rajkhowa, Chris Holland, Joselito Macabuhay Razal, Dylan Yalmar Hegh, Pablo Mota-Santiago, Peter Lynch, Benjamin James Allardyce**

M. Zaki, R. Rajkhowa, J. M. Razal, D. Y. Hegh, P. Lynch, B. J. Allardyce

Institute for Frontier Materials, Deakin University, Geelong Waurin Ponds Campus, Pigdons Road, Geelong, VIC-3216, Australia

E-mail: ben.allardyce@deakin.edu.au

P. Mota-Santiago

Australian Synchrotron, ANSTO, 800 Blackburn Road, Clayton, VIC-3168, Australia

C. Holland

School of Chemical, Materials and Biological Engineering, University of Sheffield, Sir Robert Hadfield Building, Mappin Street, Sheffield S1 3JD, U.K

Keywords: silk fibers, wet spinning, hierarchical structures, liquid-liquid phase separation, biomimicry

The remarkable toughness ($>70 \text{ MJm}^{-3}$) of silkworm silk is largely attributed to its hierarchically arranged nanofibrillar nanostructure. Recreating such tough fibers through artificial spinning is often challenging, in part because degummed, dissolved silk is drastically different to the unspun native feedstock found in the spinning gland. The present work demonstrates a method to dissolve silk without degumming to produce a solution containing undegraded fibroin and sericin. This solution exhibits liquid-liquid phase separation above 10% (wt/wt), a behavior observed in the silk gland but not in degummed silk solutions to date. This partitioning enhances the stability of the undegummed solution, delaying gelation two-fold compared with degummed silk at the same concentration. When spun under identical conditions, undegummed solutions produces fibers 8× stronger and 218× tougher than degummed silk

feedstocks. Through ultrasonication, undegummed wet spun fibers are seen to possess hierarchical structure of densely packed ~20 nm nanofibrils, similar to native silks, although completely absent from fibers wet spun from degummed silk solutions. This work demonstrates that the preservation of molecular weight, presence of sericin and stimulation of liquid-liquid phase separation underpin a new pathway to recreate a hierarchical fiber with structures akin to native silk.

1. Introduction

Silk is a model for both protein and polymer processing, manifesting in practically unmatched fiber performance in nature.^[1] Upon spinning silk proteins, fibroins, align and denature under flow, expelling water to self-assemble and consolidate into a fiber consisting of an ordered hierarchical structure dominated by tightly packed nanofibrils which is thought to contribute greatly to silk's high toughness.^[2] However much remains unknown about the exact mechanism and blueprints of natural spinning, and such structural hierarchy has yet to be faithfully reproduced in artificially spun silk fibers.

To obtain a silk solution for artificial spinning, two approaches are typically used: recombinant protein production, or solubilization of spun silk (also known as regeneration or reconstitution).^[3] Recombinant processes enable the creation of bespoke fibroin proteins but are comparatively more expensive to mass produce due to the specialist facilities required.^[4] Furthermore, current expression systems cannot yield large proteins such as the 390 kDa fibroin heavy chain produced by the commercial silkworm *Bombyx mori* (*B. mori*).^[4]

Alternatively, silk solutions can be extracted from spun silk, however its mechanical stability makes it notoriously resistant to solubilization and regeneration inevitably causes unwanted protein hydrolysis,^[5] reducing molecular weight (MW).^[6] The result is a silk solution with significantly different flow behavior to that found naturally within the spinning gland.^[7] This

gap in properties explains why attempts at artificial spinning of regenerated silks has fallen short of matching naturally spun silk.^[3] Whilst considerable efforts have gone into improving solubilization methods to minimize fibroin degradation,^[8] it has not yet been eliminated, with the degumming stage contributing most to molecular damage.^[9]

In nature, silkworms spin cocoons by co-pultruding fibroin fibers within a sericin protein matrix, forming a non-woven composite.^[10] Industrially, to reel silk fibers, sericin must be removed via the process of degumming,^[5a] typically by boiling in alkaline Na_2CO_3 .^[8a, 11] For millennia this has been the standard practice for textile silk, and this knowledge inevitably shaped the past century of silk research, infusing the field with a consensus that degumming was a necessary evil required to obtain purified regenerated fibroin.

Yet ideally, a silk solution that serves as an artificial feedstock should retain the composition and molecular integrity of silk to enable the recreation of the hierarchical features seen in a natural silk. Therefore, we hypothesized that the commonplace removal of sericin makes it impossible to fully understand the behavior of the natural spinning system, where both fibroin and sericins are present and appear to interact and influence the structure of one another in ways not currently understood.^[12]

This study describes a simple, non-toxic approach to dissolve undegummed silk directly from cocoons with negligible degradation, producing an artificial spinning feedstock that retains sericins. The resultant solution, referred to here as regenerated undegummed silk solution, exhibits liquid-liquid phase separation (LLPS) and can be wet-spun into fibers with a nanofibrillar hierarchy and better-than-natural mechanical properties. By focusing on preserving silk's natural properties and systematically investigating the stages of the spinning process, this work provides a significant contribution to understanding natural spinning and

paves the way for low-energy spinning methods to produce regenerated fibers with remarkable properties.

2. Results and discussion

2.1. Un-degummed silk solution properties

Our approach first involves cutting undegummed cocoon fibers into small snippets, greatly increasing the surface area, before dissolving in 13.6 M supersaturated lithium bromide (LiBr). This high molarity LiBr must be dissolved using hot (60 °C) water as it precipitates at room temperature (RT). This unique combination enables us to solubilize undegummed fibers without the need for any further damaging degumming process (**Figures S1** and **S2**).

2.1.1. Molecular weight analysis

Regenerated undegummed silk (RUS) solution properties were evaluated against classically degummed regenerated silk fibroin (RSF) (**Figure 1**).^[13] SDS-PAGE MW analysis of RUS revealed three distinct bands attributed to fibroin, with bands at approximately 30 kDa and 25 kDa representing the P25 and light chain, respectively (**Figures 1A** and **S3A**).^[5b, 14] The high MW band was estimated to be 420 kDa. Although slightly higher than the predicted 390 kDa, this aligns with reported MW of native gland silk using SDS-PAGE.^[5b, 15] These RUS bands closely match those directly extracted from *B. mori*'s spinning gland,^[15] and implies that the N-termini has not been lost as recently observed in standard regeneration protocols,^[16] suggesting that through this method fibroin remains largely intact during dissolution.

In contrast, RSF showed extensive smearing between 268 and 71 kDa, a less intense 25 kDa light chain band, and lacked the 30 kDa P25 band. Such smearing is typical for alkaline degummed RSF, due to significant hydrolysis leading to degradation into a broad range of MWs.^[6b, 8b]

Although RUS is assumed to contain sericin, no obvious bands were detected on the gels, likely due to its relatively low concentration, comprising only 25–30% (wt/wt) of the cocoon weight. To detect sericin, a gel was loaded with 30, 60 and 120 μg of protein per well, revealing additional bands (**Figures 1B** and **S3B**). Due to the similarities in amino acid composition between sericin and fibroin, definitive assignment of these bands is challenging. However, their MWs align with those reported for sericin suggesting its presence after dissolution and dialysis.^[17] This is further supported by Fourier transform infrared spectroscopy showing peaks attributed to carboxylic acids (COO^- symmetrical stretching and C-O stretching),^[18] aspartic acid and glutamic acid, at ~ 1400 and $\sim 1060\text{ cm}^{-1}$, characteristic of sericin but absent in fibroin (**Figure 1C**).^[17b, 19] Notably, bands above 200 kDa corresponding to intact sericin were not detected; instead, slight smearing between 100 and 400 kDa may indicate some degradation. While degradation temperatures have not been precisely determined, the denaturation endotherms for fibroin and sericins are approximately $62\text{ }^\circ\text{C}$ and $40\text{--}45\text{ }^\circ\text{C}$, respectively.^[20] Since protein degradation is more likely to occur in a denatured state, and the dissolution temperature was maintained below the denaturation endotherm of fibroin but above that of sericin, it suggests sericin degradation during dissolution.^[21] Further studies are planned to confirm this hypothesis.

2.1.2. Rheology

Rheology was used to further characterize the mechanical properties of the solutions. As expected, RSF viscosity increased with increasing concentration (**Figure 1D**), and shear-thinning viscoelastic behavior was observed across all concentrations, typical of an aqueous polymeric network.^[22] In contrast, RUS exhibited markedly different behavior, with relatively high viscosity and more pronounced shear thinning observed at 5% (wt/wt) RUS, which decreased significantly at 10% RUS (**Figure 1E**). Upon closer inspection under optical microscopy, LLPS was identified at concentrations above 5% (**Figure 1H**). At 15% RUS,

viscosity increased slightly, and at 20% RUS, viscosity fully recovered, almost equivalent to RSF, while the number of phase condensates also increased, the presence of which was not observed in RSF (**Figure 1G**).

It is believed that LLPS drives the protein into phase condensates, while diluting the surrounding liquid phase, thereby causing the observed reduction in bulk viscosity as measured by rheology. Although LLPS initially reduces viscosity, an increase in viscosity was eventually observed at higher RUS concentrations. This could be due to the increasingly dense packing of the phase condensates, a behavior commonly observed in emulsions.^[23] Alternatively, it is possible that as concentration increases above 15%, the concentration within the phase condensates reaches a plateau while the concentration in the surrounding liquid phase continues to increase, thereby increasing bulk viscosity.

2.1.3. Comparison to synthetically induced LLPS in RSF

The liquid-like behavior of phase condensates, which are a dynamic polymeric network, has been linked to the sticky reptation model.^[24] This model describes silk as a randomly coiled, worm-like polymer with “sticky” groups that reversibly and dynamically interact with neighboring chains through various forces such as hydrogen bonding and metal ion bridging. LLPS is believed to reduce viscosity and act as a switchable intermediate that facilitates fiber formation.^[25]

Silk LLPS has been previously modeled using synthetic molecular crowders like dextran and polyethylene oxide (PEO).^[13, 26] RSF, commonly used but lacking sericin, is often studied by combining it with polyethylene oxide (PEO) as a synthetic alternative to sericin, artificially inducing phase separation in degummed fibroin.^[13, 27]

To confirm that the decrease in RUS viscosity correlates with the onset of phase separation, we compared RUS to PEO-blended RSF (RSF-PEO), which also exhibited decreased viscosity and

simultaneously formed phase condensates as a function of concentration (**Figures 1F and 1I**). The phase condensates in RUS displayed behaviors similar to other LLPS polymers.^[25a, 28] they flowed independently and occasionally merged into larger droplets (**Figures 1J and Video S1**). Furthermore, shear was observed to elongate the spheroidal condensates into a teardrop shape (**Figures 1K and 1L and Video S2**), a phenomenon observed in other LLPS systems,^[29] providing potential insights into how phase condensates evolve into fibrils during natural spinning.

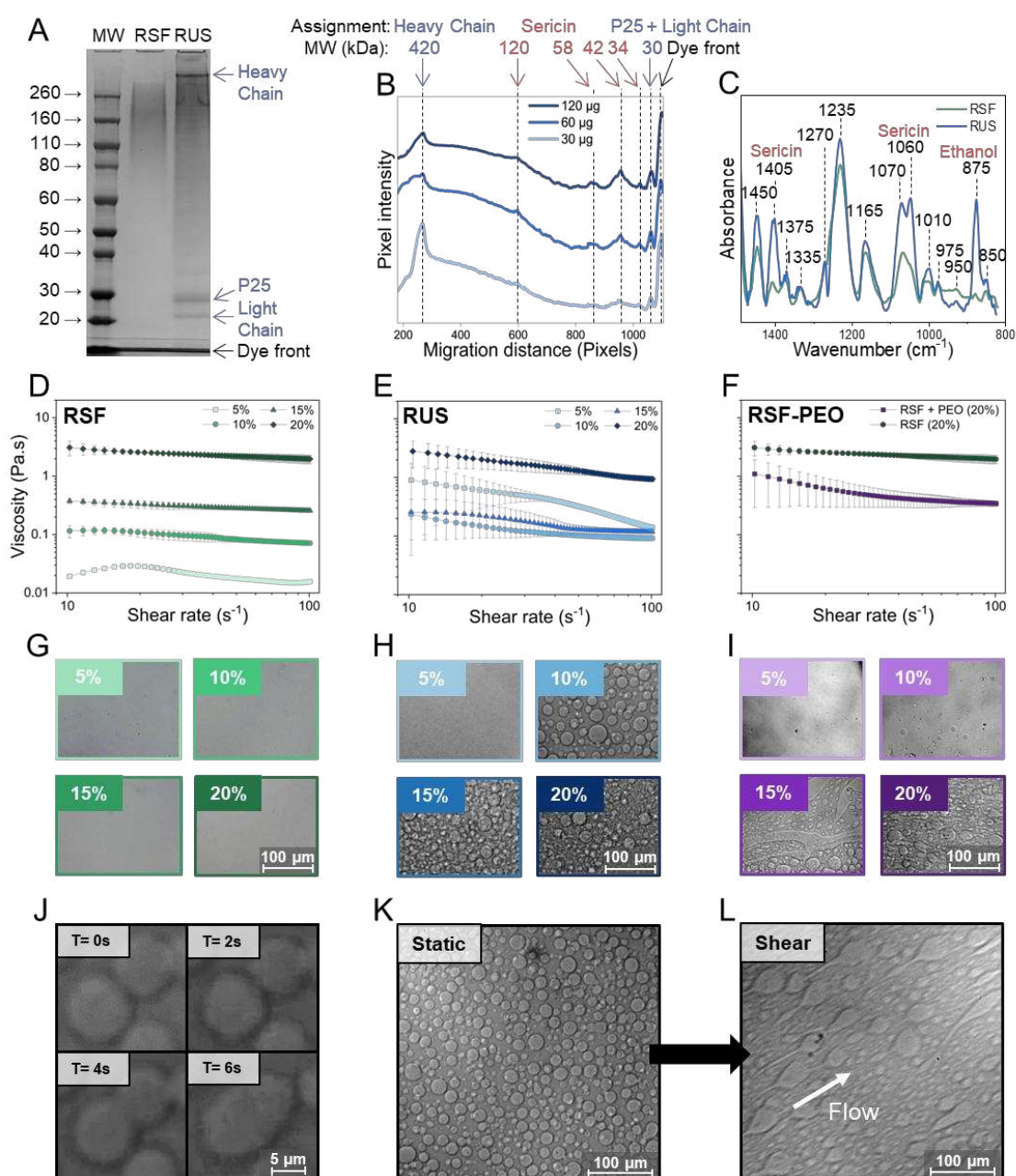


Figure 1. Solution properties of RUS and RSF solutions. A) 4-12% gel of RUS and RSF.

Identification of sericin in RUS using B) a 3-8% gel at 30, 60, and 120 μg loading, plotted as pixel intensity as a function of migration distance (**Figure S3B**), and C) FTIR spectra of ethanol-cast films. The MW ladder was used to create a standard curve allowing sample band MWs to be identified. Fibroin and sericin are labelled in blue and red, respectively. Viscosity as a function of shear of D) RSF, E) RUS, and F) 20% RSF-PEO, G – I) and their respective optical images at varying concentrations, where viscosity is mean of duplicate readings \pm standard deviation (SD). Optical images of 10% RUS phase condensates J) coalescing into a larger droplet over time, and droplet morphology K) before and L) after shear.

2.2. Spinning regenerated undegummed silk fibers

2.2.1. Fiber morphology and mechanical properties

Having determined the fundamental solution properties, we continuously spun regenerated silk fibers by extruding 20% RSF or RUS through a coagulation bath containing 30% (wt/v) $(\text{NH}_4)_2\text{SO}_4$, achieving lengths up to 30 meters (**Video S3**). The RSF fiber surface appeared relatively smooth with a fine porous core and thick skin, a morphology commonly observed in wet-spun silk fibers (**Figure 2B**).^[30] In contrast, RUS fibers developed a highly irregular multi-lobed morphology and exhibited tightly packed nanofibrils ~ 20 nm wide (**Figure 2C**), closely resembling natural *B. mori* fibers (**Figure 2D**). To identify the location of proteins within RUS fibers, cross-sections were stained and imaged under confocal microscopy (**Figure S5**). Although sericin and fibroin were easily distinguishable within cocoon baves, RUS and RSF showed no clear difference. Future work will further probe the fibroin and sericin distribution within RUS fibers.

Mechanical testing and statistical analysis revealed that RUS fibers displayed significantly better properties compared to degummed RSF silk (**Figures 2E to 2I**). The RSF fibers were

weak and brittle, achieving a stress and strain-at-break of only 70 MPa and 2.2%, respectively, even after post-spinning drawing and annealing, typical of fibers wet-spun from degummed silk.^[3] In contrast, the RUS fibers had a breaking stress of almost 600 MPa and a remarkably high strain-at-break of 47%. Under the same conditions, RUS fibers were more than 8 times stronger, 21 times more extensible, 5 times stiffer and, most impressively, 218 times tougher than RSF fibers. Compared to cocoon brins, RUS fibers had similar strength but were 2.1 times more extensible, 1.7 times stiffer, and 2.3 times tougher.

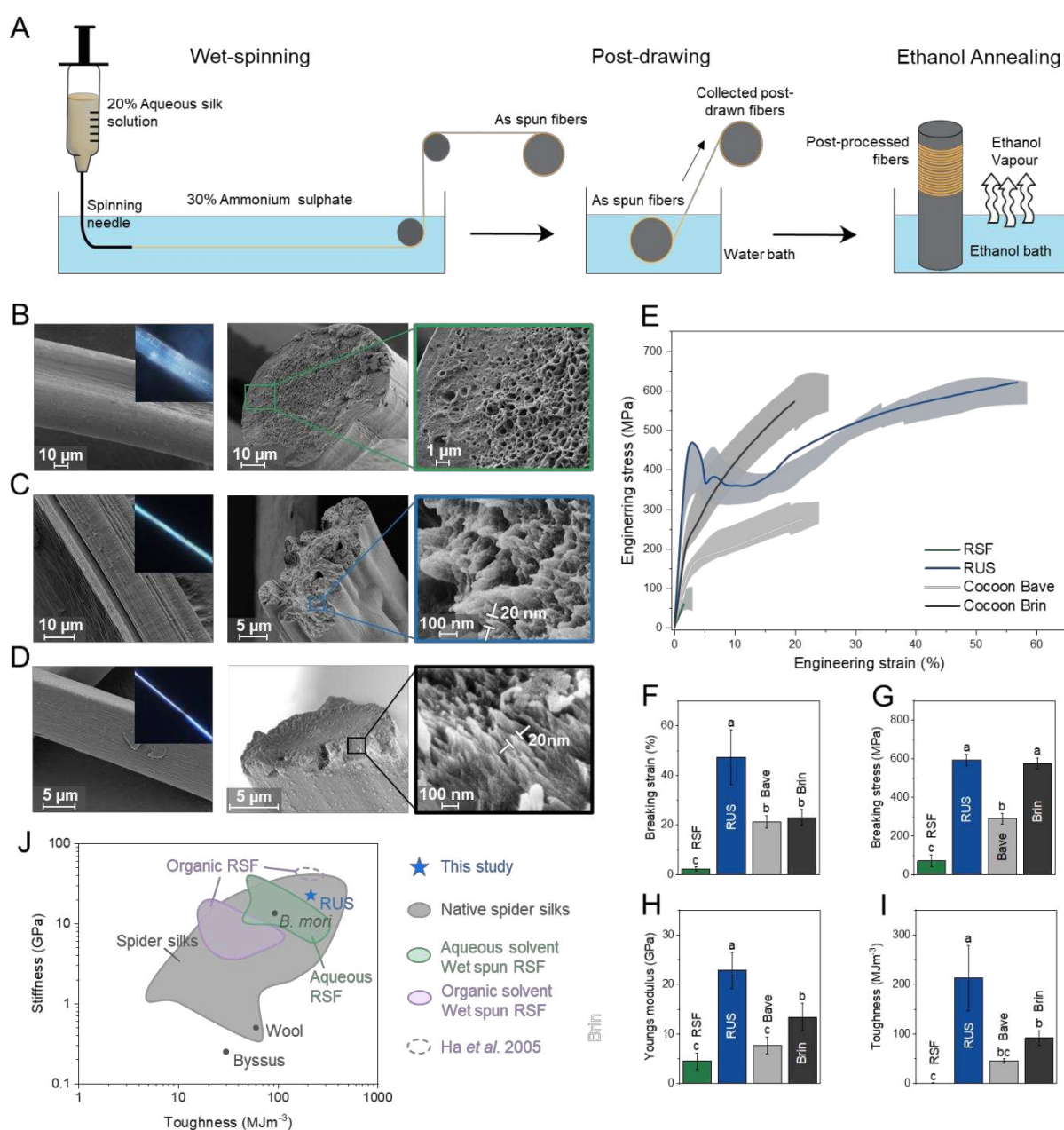


Figure 2. Morphology and mechanical properties of post-processed wet spun fibers. A) Schematic detailing wet-spinning and post-processing. SEM and polarized optical microscopy (inset) images of the fiber surface and freeze fractured cross-sectional SEM images at low and high magnification for B) RSF and C) RUS and D) *B. mori* silk cocoon brins. E) Representative stress-strain curves with shaded area demonstrating SD alongside the average F) strain-at-break, G) tensile strength, H) stiffness, and I) toughness, where $n=5$, error bars = SD, results are normally distributed (Shapiro-Wilk), and groups are significantly different (Tukey, $p<0.05$). J) Ashby plot comparing the stiffness and toughness of RUS relative to other protein fibers (Ashby plot references and raw data can be found in SI). Dashed circle highlights the fiber properties of Ha *et al.*,^[31] of which findings have yet to be repeated.^[3]

2.2.2. Confirmation of fibrillar hierarchy

To confirm that these fibrillar structures were not merely artifacts resulting from SEM sectioning, we subjected RUS, RSF, and native silk fibers to ultrasonication (**Figure 3**). In natural silk fibers, ultrasonication is known to reveal microfibrillation,^[32] partially releasing fibril bundles. Sonication of RUS resulted in the peeling of 100-400 nm microfibrils from the larger fiber and the formation of a network of exfoliated fine nanofibrils (5-30 nm) in the supernatant (**Figures 3B, 3D and S7**). In contrast, RSF fiber sonication revealed a porous network, with the supernatant containing an amorphous mixture of nanofibril-free micron and nanoscale particles (**Figure 3A**). The presence of RUS micro- and nanofibrils is intriguing as it closely matches the structural hierarchy found in natural silk (**Figures 3C and S6**).

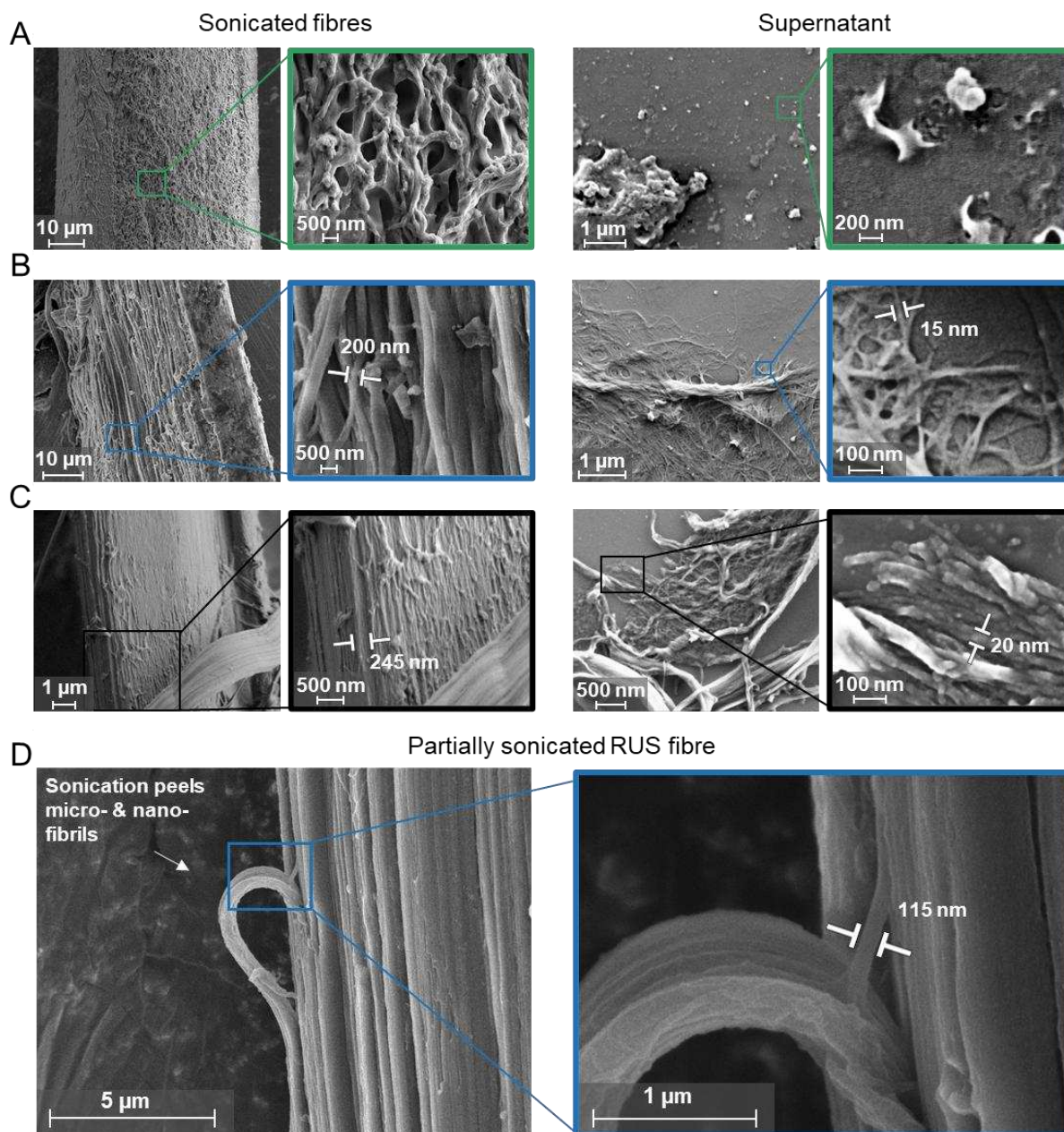


Figure 3. Confirmation of fibrillar hierarchy via ultrasonication. SEM images of sonicated fibers and supernatant at low and high magnification. Sonication of A) RSF exposes a porous disordered matrix, while B) RUS and C) cocoon fibers micro- and nano-fibrils are D) peeled from their parent fiber.

2.2.3. Crystallinity and structural alignment

Although RUS exhibited a similar fibrillar nanostructure to cocoon brins, the mechanical properties differed significantly. Therefore, secondary and tertiary structures were

characterized by FTIR, polarized Raman and synchrotron X-ray scattering (**Figure 4**). The overall FTIR spectra of RUS and cocoon brins appeared almost identical, but RSF had additional FTIR peaks at ~ 1100 and ~ 1420 cm^{-1} (**Figure 4A**). These peaks result from N-H and S-O stretching; this indicates that RSF may retain residual $(\text{NH}_4)_2\text{SO}_4$ after washing. Since all fibers were thoroughly washed following the same protocol, the presence of residual salt in RSF is likely due to the high fiber porosity observed in SEM images. Salt contamination in RSF was confirmed in Raman with a sharp peak at 975 cm^{-1} attributed to SO_4^{2-} stretching (**Figures 4B**). Together this also implies that standard RSF protocols may bind more tightly to salts than our RUS approach and therefore encounter more difficulties in purification required for biomaterial applications. Proportionally cocoon brins exhibited slightly more β turns, while RUS and RSF had slightly more random coils (**Figures 4C** and **S8**). As β turns are the connection between anti parallel β -sheets, the larger number may reflect differences in crystallite size between RUS and cocoon brins. On the other hand, RSF likely has less β turns due to degradation.

Polarized Raman was used to estimate the molecular alignment relative to the fiber axis (**Figures 4B** and **4D**). The intensity ratio of the amide I peak (I_{XX}/I_{ZZ}) indicates the orientation of the secondary structures, with higher ratios indicating greater alignment. Cocoon fibers were the most aligned, with an alignment ratio of 2.01, consistent with reported values.^[33] In contrast, RSF fibers had the lowest alignment ratio of 1.18, and RUS had a ratio of 1.46. This indicates that under identical spinning and drawing conditions, the unique composition of RUS facilitates a greater degree of structural organization than RSF during spinning.

Wide-angle X-ray scattering (WAXS) analysis was used to provide further indication of alignment within the fibers (**Figures 4E**). Cocoon brins exhibited sharp reflections, indicating an anisotropic fiber structure, while RSF only diffraction rings were recorded, indicating lack of preferential orientation (isotropy). In contrast the RUS exhibited an intermediate broad but

well defined reflections, indicating some degree of preferential orientation, evident by the diffraction arc pattern corresponding to (020). Furthermore, the orientation factor at (020) was calculated using Herman's orientation function,^[34] and crystallite size was estimated from the full width at half height (FWHM) of the (020) peak. The determined orientation factor was highest for the cocoon fibers (0.97), followed by the RUS (0.84) and complete isotropy (0) for RSF fibers (**Figure 4F**). Interestingly, RUS had a crystallite size significantly smaller than cocoon brins (1.16 vs 3.43 nm) while RSF had a very large crystallite size (24.38 nm) (**Figure 4G**). The large difference in crystallite size likely contributes significantly to the observed mechanical properties. The superior mechanical properties of spider silk compared with *B. mori* cocoon brins are believed to be linked to the smaller crystallites.^[35] The failure mechanism for large crystallites (3-8 nm) is anticipated to create a brittle fiber, while small crystallites (<3 nm) allow for the regeneration of hydrogen bonds during stretching, producing a tougher fiber.^[36]

While crystal structure can be determined by WAXS, the existence of voids can be characterized by small-angle X-ray scattering (SAXS).^[37] The SAXS pattern for cocoon fibers exhibited an ellipsoidal scattering, indicating the presence of voids aligned parallel to the fiber direction (**Figures 4H** and **4I**). In contrast to the cocoon fibers, RSF exhibited a diamond shaped scattering, indicating also the presence of voids in both lateral and axial directions. RUS exhibited ellipsoidal scattering, indicating the presence of voids also aligned along the fiber axis. Additionally, a horizontal long period of 5.1 nm was present in RUS but absent in RSF and cocoon fibers. The observed SAXS horizontal long period may indicate lateral periodic spacing between the voids in RUS, occurring between the nanofibrils.^[38] In general, SAXS patterns agree with the presence of voids as observed within sonicated RSF and RUS fibers (**Figure 3**).

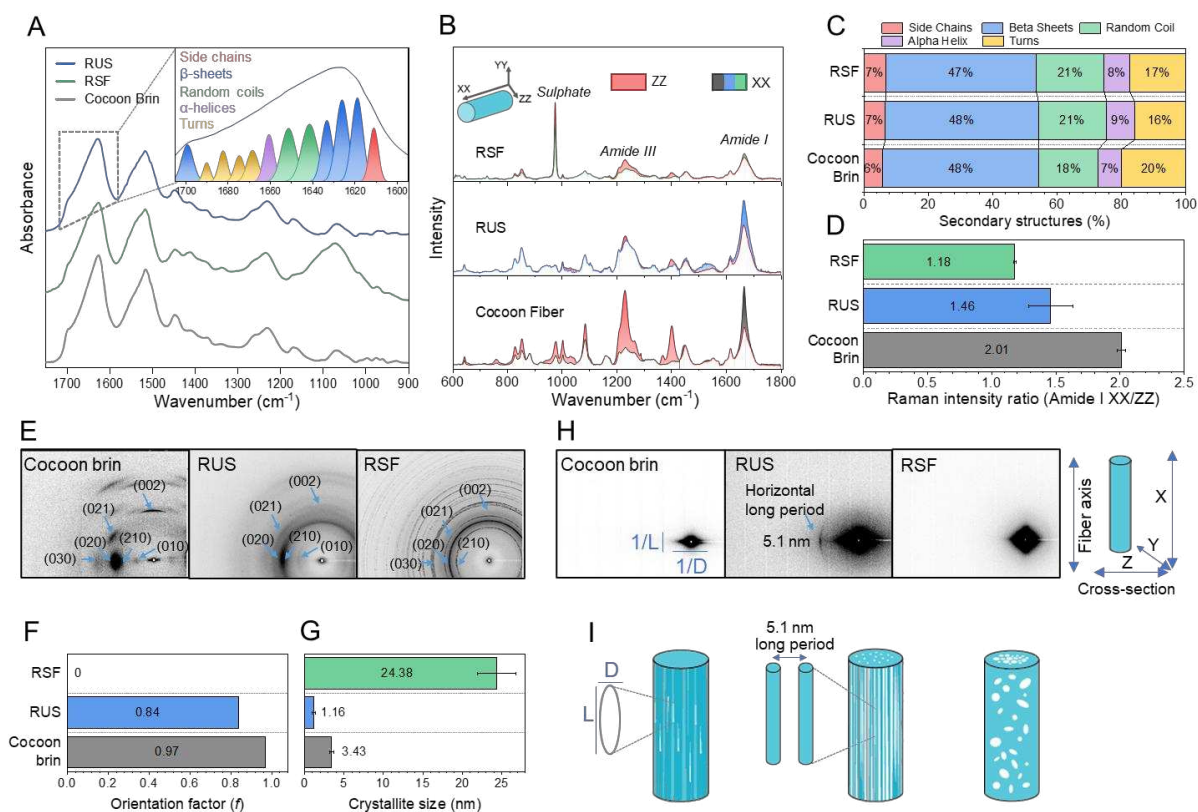


Figure 4. Crystallinity and structural alignment of Cocoon brins, RUS, and RSF fibers. A) FTIR spectra with a deconvoluted Amide I peak (inset). B) Polarized Raman spectra of the Amide I peak taken parallel (XX) and perpendicular (ZZ) to the fiber axis. C) Secondary structure analysis obtained by integrating the deconvoluted curves in A. D) Intensity ratios of the Amide I peak in B. E) 2D WAXS patterns used to identify the F) Orientation factor and G) crystallite size. H) 2D SAXS patterns used to create I) schematic of voids within fibers.

The dramatic improvement in mechanical properties of RUS compared to RSF may be due to several factors. Firstly, the higher MW of fibroin in RUS enables a greater degree of physical entanglement and, therefore, increased intermolecular interactions.^[39] Simultaneously, the presence of sericin may act as a plasticizer making the fiber more resistant to crack propagation.^[40] Such a plasticizing effect has been reported for fibers electrospun using blends of degummed fibroin and extracted sericin, where sericin facilitated fibroin β -sheets through intra-molecular hydrogen bonding, producing a tougher material.^[41] Additionally, the fibrillar

nanostructure of RUS may contribute to its high toughness, as the structural hierarchy of natural silk is believed to be key to its toughness.^[2] The organization of silk into nanofibrils can dissipate breaking energy through substantial complementary intramolecular hydrogen bonds and prevent crack propagation.^[2, 42] In contrast, the randomly dispersed voids present within RSF likely induce crack propagation, creating an extremely brittle fiber.^[43] Furthermore, natural silk fibers contain packing defects due to spinning irregularities.^[44] As RUS fibers were spun with controlled, uniform speed and draw, defects were likely avoided, resulting in better fibers.^[45] Moreover, RUS fibers exhibited a high yield point followed by a sharp drop in stress indicative of the reorganization of disordered structures into ordered and from necking.^[8b, 45] To better explain this, SAXS/WAXS analysis was performed at different degrees of fiber strain; by overlaying this onto the tensile curve further insight into the relationship between structural changes under mechanical load can be determined (**Figure 5**). Although orientation increased slightly with strain, the crystal size did not significantly change, suggesting that only reorientation of the crystallites took place. As crystal alignment tends to drive the modulus, cocoon brins are anticipated to be stiffer.^[46] However, RUS fibers were stiffer, indicating that alignment of the nano- and micro-fibrils also had a key influence on the observed modulus of silk fibers (**Figure 5F**). This is further supported by the disappearance of the long period, as observed in the SAXS pattern after the yield point, which indicates realignment of entangled nano- and micro-fibers and the dissipation of interfibrillar voids resulting in the necking observed (**Figures 5B and 5D and S11**).^[47] Additionally, strain-hardening was prominent in post-processed RUS fibers, with effects analogous to silk attributed to intramolecular beta sheets.^[48] As intramolecular β -sheets unfold, hydrogen bonds regenerate allowing energy to be dissipated throughout the β -sheet significantly increasing its strength.^[36] It is noteworthy that the post-yield drop and intramolecular beta sheets depend on reeling conditions, suggesting significant potential to produce fibers with properties far exceeding those of natural or synthetic high-performance fibers.

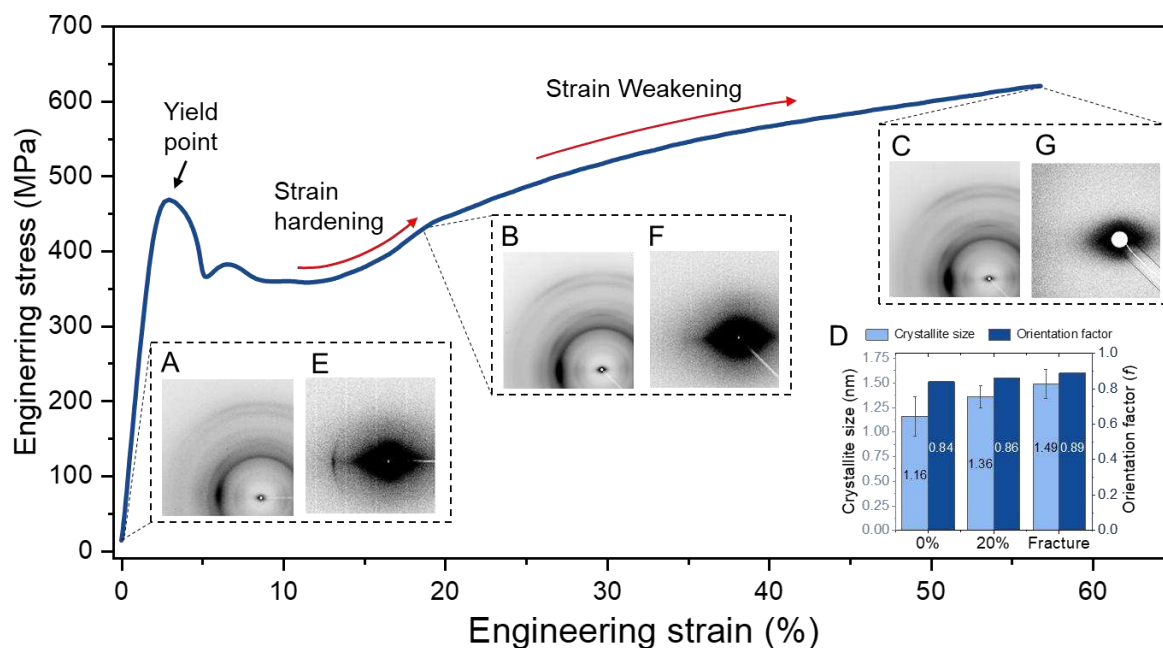


Figure 5. RUS fiber deformation. Annotated stress-strain curve of RUS alongside 2D WAXS (A to C) and 2D SAXS (E to F) patterns at 0%, 20%, and fracture. WAXS was used to obtain D) crystal size and orientation factor.

Other studies have demonstrated artificially spun fibers with a nano fibrillar structure, but these fibers lack toughness.^[47, 49] Conversely, fibers with high toughness have also been reported, yet these lack nanofibrillar structure.^[39, 50] To the authors' knowledge, the present work represents the first evidence of the development of tough nanofibrillar fibers in wet-spun silk using an aqueous solution.

2.3. Further examination of phase separation

Having established a system capable of producing native-like fibers, we proceeded to further understand the impact of phase separation on dope stability, as additive-free (i.e. salts and polymers) LLPS has not been reported for regenerated silk solutions.

2.3.1. Stability

Although the formation of phase condensates in the silk gland has been hypothesized to prevent gelation,^[13, 51] stabilizing highly concentrated solutions, this has never been experimentally evaluated. Therefore, we investigated the sol-gel transitions of RUS up to 25%, the concentration found in the silk gland (**Figures 6A** and **6E**).^[15] Remarkably, as the concentration increased, the RUS solution became more stable - a behavior opposite to RSF, which gels more rapidly at higher concentrations.^[52] For example, the 5% RUS solution, which did not undergo phase separation, gelled after ~5 days, whereas the phase separated 15% RUS took more than 20 days to gel (**Figure 6A**). At concentrations of 20% and higher, RUS did not gel at all for over 25 days; instead, it gradually dried as water evaporated from the well, leaving behind a membrane with spherical craters similar in size to the observed condensates in the dried films (**Figure 6E**). In comparison, 20% RSF gelled after only 8 days (**Figure 6B**).

The inhibition of gelation and the retention of silk condensates after film formation further indicate the remarkable stability of RUS solutions at high concentrations, especially considering that the actual silk concentration would significantly increase as water evaporates. The observed stabilizing effect of LLPS may explain why single-phase RSF gels prematurely at high concentrations, while LLPS silk in the spinning gland remains stable. Additionally, previous findings suggest that increasing sericin concentration improves the stability of degummed fibroin solutions and is likely contributing to the stability of RUS.^[12b] Since the sericin/fibroin ratio remained unchanged in our study, its consistent influence on stability suggests that the observed improvements are likely due to the phase separation. However, it should be noted that the sericin/fibroin concentration in RUS remains unknown. Following dissolution and dialysis, some undissolved material was removed during processing, and the SDS-PAGE of this material showed a MW distribution similar to that of the dissolved fraction (**Figure S12**). Assuming complete sericin dissolution, the fibroin content in RUS is estimated

to be 70 to 80% of the total solids content, based on the established fibroin-to-sericin ratio in *B. mori* cocoons. For example, the 25% RUS would contain approximately 17.5 to 20% fibroin and 5 to 7.5% sericin.

To further understand the stabilizing effect of LLPS, we added PEO to re-introduce LLPS to degummed silk. Although the phase condensates in RSF-PEO appeared superficially similar to those in RUS, the addition of PEO significantly decreased solution stability; solutions > 5% demonstrated phase separation and gelled rapidly in less than 5 days (**Figure 6C**). This suggests that PEO may not model silk behavior in the spinning gland.^[53] Furthermore, PEO is known to increase the dehydration enthalpy of condensates leading to denser droplets,^[54] which likely accelerates silk gelation. In contrast, sericin significantly delays fibroin gelation through reversible hydrogen bonding.^[12b] It is speculated that RUS phase condensates represent a dynamic, ever-changing polymeric network, as described by the sticky reptation model,^[24a, 24b] facilitating fiber formation while simultaneously increasing stability before spinning. However, this dynamic may not apply to RSF-PEO due to PEO's poor hydrogen bond donor capabilities compared to sericin.^[55] This implies different phase separation mechanism for RUS and RSF-PEO, making PEO an unsuitable model for sericin. Sericins are amphipathic proteins with varying MWs and moieties vastly different from the simple repetitive glycol structure of PEO. Therefore, sericin would not behave similarly to PEO in stability tests. Future evaluations of fibroin with different sericin fractions could provide valuable insights into significantly improving silk stabilization.

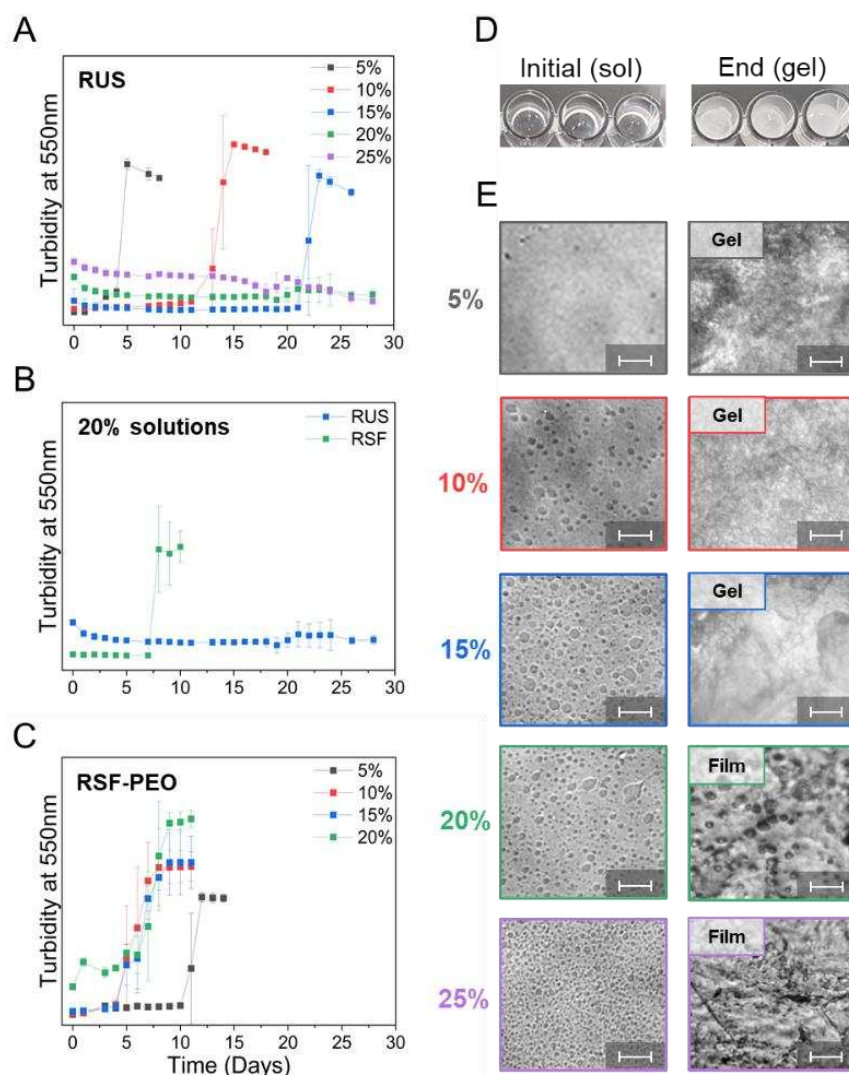


Figure 6. Turbidity measurements over time for A) RUS, B) direct comparison of 20% solutions, and C) RSF-PEO, where $Y_{\text{error}} = \pm\text{SD}$. D) Macroscopic images illustrating the typical transition of solution to a gel for all silk solutions studied and E) Optical images of RUS solutions at the beginning and end of turbidity measurements. scale bar: 20 μm .

2.3.2. Examination of RUS phase condensates

The underlying cause of phase separation in regenerated undegummed silk is not immediately obvious. As mentioned earlier, RUS differs from RSF in two key aspects – the much higher MW of fibroin and the presence of sericin. Determining the contribution of these factors to silk LLPS is challenging; however, both are likely significant. In other systems, factors such as

polymer length,^[56] molecular crowding,^[26] and the alternating hydrophobic and hydrophilic amino acid sequences,^[28a] have been reported to influence the formation of phase condensates.

To identify the location of proteins, condensates were probed using staining with FITC, a fluorescent dye that binds efficiently to primary hydroxyl and amine groups in proteins. Sericin, containing significantly more serine, threonine, tyrosine, asparagine, and glutamine amino acids (>40 vs ~18 mol%),^[17a, 17c] was predicted to bind favorably to FITC. After the reaction, no difference in phase separation behavior was observed between labeled and unlabeled samples. In the case of RUS, the surrounding matrix showed strong fluorescence while the phase condensates appeared dark, suggesting that sericin may primarily reside in the continuous phase (**Figure 7A**). However, the P25 and fibroin light chain also contain a significant portion of primary hydroxyl and amine groups,^[57] and thus could also fluoresce brightly.

Further investigation involved processing the stained solution through a gel and imaging it under fluorescent light (**Figure 7B**). A distinct band fluoresced brightly at ~25 kDa in RUS, which was notably weaker in RSF even at higher concentrations. After fluorescent imaging, the gel was conventionally stained with colloidal blue and re-imaged under visible light (**Figure 7C**), confirming the presence of the 25 kDa band in both solutions. Traditionally, this band is attributed to the fibroin light chain. However, as the 25 kDa band in RSF shows no apparent degradation yet does not fluoresce, it suggests that either degumming has chemically altered the light chain without reducing its MW, or there is a sericin component present at a similar MW as the fibroin light chain. Since degumming hydrolyses proteins indiscriminately,^[6a] it is unlikely that the light chain would undergo chemical changes without a reduction in MW; thus, the fluorescing band likely corresponds to sericin. Despite identifying this particular sericin in the dilute phase, it remains inconclusive regarding the localization of the other proteins using this method.

SEM was used to examine the morphology of phase condensates for additional insights (**Figures 7D** and **S13**). Condensates ranging in size from 5 to 100 μm were observed, although some larger droplets were likely flattened during sample preparation, exaggerating their radius (see methodology). A distinct boundary separated the two phases, revealing clear differences between the phase condensates and the bulk phase. The condensates appeared smoother and more homogenous, while the bulk phase consisted of a rough, heterogenous aggregation of spherical particles.

Based on this evidence, we propose the following mechanism for LLPS-facilitated nanofibril formation (**Figure 7E**). Above the 10% critical silk concentration, LLPS droplets form as a result of sericin molecular crowding. At the same time, reversible hydrogen bonding at the fibroin-sericin interface stabilizes the mixture, preventing gelation; such behavior has been observed previously.^[12b] The LLPS droplets remain fluid, spontaneously and reversibly merging and dividing (**Video S1**). Under shear, these dynamic droplets elongate and organize into teardrop shapes, creating axial stresses that generate a tail which is subject to further extensional flow that serves to align and denature silk proteins into nanofibrils (**Video S2**).^[58] By acting as a molecular crowder and maintaining the droplet boundary through hydrogen bonding, sericin ultimately maintains the droplet boundary to enable the formation of discrete nanofibrils within the final, larger fiber.

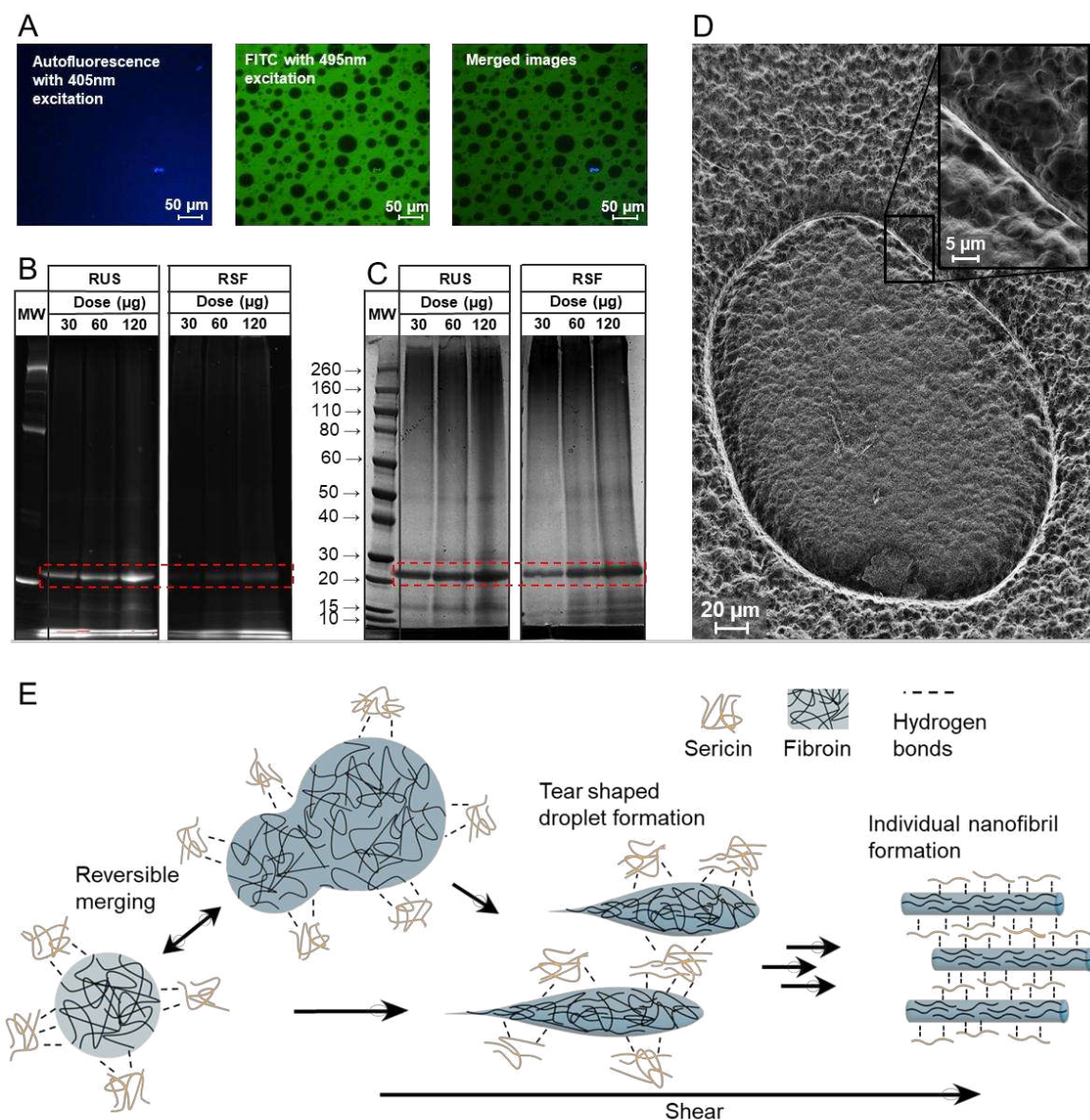


Figure 7. Detailed examination of RUS phase condensates and its potential applications. A) Confocal images of RUS solution at 405 nm to excite autofluorescing proteins, at 495 nm to excite proteins tagged with FITC, and the merge of the two images. B) 4-12 % gel of FITC stained RUS and RSF imaged under fluorescent light and C) visible light after Coomassie staining. D) SEM image of a larger RUS phase condensate with close-up of the droplet boundary (inset). E) Schematic illustration of the proposed nanofibril assembly mechanism.

2.3.3. Additional applications of RUS

3. Conclusion

While numerous studies have highlighted the roles of pH,^[60] metal ions,^[61] and flow,^[62] this work suggests that both retaining fibroin's MW and the presence of sericins may be equally critical in understanding the mechanism for spinning silk with structural hierarchy and native-like properties. The degumming-free dissolution method developed in this study produces an aqueous regenerated silk with native-like MW, which undergoes additive-free LLPS as a function of concentration. The improved gelation stability resulting from phase separation is significant, providing a possible explanation for why classical single-phase degummed silk becomes unstable at high concentrations.

With respect to spinning, regenerated RUS fibers were continuously spun and consisted of ~20 nm nanofibrils, akin to native silk. The post-processed fibers were 2.3 times tougher than natural silk and 218 times tougher than regenerated degummed silk, attributed to the fibrillar structure and higher MW. Such fiber structures has only been achievable with short fiber lengths which exhibit poor mechanical properties.^[47, 49] However, the mechanism underlying the formation of fibrillar micro- and nano-structures is still not fully understood, with further investigation needed to determine whether phase separation, high fibroin MW, or their combination is necessary to produce hierarchical fibers.

In summary our research introduces a new platform of artificial silk which enables investigation of silk LLPS without external variables such as salts, thereby accelerating research on silk spinning mechanisms and potentially shedding light on other protein fibril mechanisms, such as amyloids in neurodegenerative diseases.

4. Experimental section/Methods

Chemicals and materials: Reeled, undegummed fibers from bivoltine *Bombyx mori* (*B. mori*) cocoons were purchased from the SRR Silk Reeling Unit (Ramanagara, Karnataka, India) and

cut into 2 mm snippets using a Pulverisette 25 power cutter mill (Fritsch, Idar-Oberstein, Germany). Lithium bromide (LiBr, 99%), sodium carbonate (Na_2CO_3 , 99.5%), polyethylene oxide (PEO, 10 kDa), and ammonium sulphate ($(\text{NH}_4)_2\text{SO}_4$, 99%) were purchased from Sigma-Aldrich (St Louis, MO, USA).

Sodium carbonate degumming of B. mori silk: For Na_2CO_3 degumming, *B. mori* silk fibers were degummed using 500 mL aluminum pots in an Ahiba IR Pro rotary dyeing machine (Datacolor, Lawrenceville, USA) with a raw silk (g): liquor (ml) ratio of 1:50. Raw silk was degummed for 30 minutes at 98 °C using 0.2% (wt/v) Na_2CO_3 . The degummed silk was washed several times with deionized water and then dried at 60 °C in a fan forced oven. Weight loss was calculated using a previously reported method,^[6b] with slight modification requiring the conditioning of samples for 24 h at 21 ± 2 °C and $65 \pm 2\%$ relative humidity (RH) before each weight measurement.

Preparation of regenerated silk solutions: For RSF, Na_2CO_3 degummed silk was dissolved in 9.3 M LiBr solution with a raw silk (g): liquor (ml) ratio of 1:7.5 at 60 °C for 40 minutes. RUS was prepared by dissolving finely cut raw silk in 13.6 M LiBr solution with a raw silk (g): liquor (ml) ratio of 1:15 at 60 °C for 6 hours. Due to 13.6 M supersaturated LiBr solution precipitating at room temperature (RT), the solution was prepared by dissolving LiBr in hot water (60 °C). The solutions were dialyzed using 3.5 kDa MWCO dialysis tubing in a custom-made flowing deionized water bath for 3 days at 4 °C. To remove insoluble fractions, solutions were filtered through muslin butter cloth and then centrifuged at $7000 \times g$ for 10 minutes at 4 °C. Solutions were then concentrated, using a previously described method,^[39] where the solution was added to 3.5 kDa dialysis tubing and left to dry under airflow in a fume hood, gradually increasing the concentration. The concentration (% wt/wt) was calculated gravimetrically by drying 2 g at 60 °C for a minimum of 3 hours and weighing the dried film. Although it was possible to

concentrate RUS to 25%, RSF prematurely gelled upon concentration to 25% and was thereby limited to a maximum concentration of 20%.

To compare liquid-liquid phase separation (LLPS) inherent in RUS, a stock solution of LLPS induced RSF was prepared following previously described methods with minor deviations.^[13, 27a] Briefly, 10 % wt/wt PEO was added to RSF (RSF-PEO) at a ratio of 90/10 (RSF/PEO) and gently mixed to prevent shear-induced gelation.

Molecular weight distribution: The molecular weights (MWs) of the RSF and RUS solutions were evaluated using sodium dodecyl sulphate polyacrylamide gel electrophoresis (SDS-PAGE) using an Invitrogen Mini gel tank (ThermoFisher, Waltham, MA, USA) coupled with a PowerPac Basic power supply (Bio-Rad, Hercules, CA, USA). Silk solutions were diluted to 2.4, 4.8, and 9.6 $\mu\text{g}/\mu\text{l}$ with Milli-Q water. A 12.5 μl of the diluted solution was further diluted with 6.25 μl NuPAGE LDS sample buffer, 2.5 μl NuPAGE Reducing Agent and 3.75 μl of Milli-Q water. Denaturing was done at 70 °C, 750RPM for 10 minutes. Subsequently, 25 μl of the denatured silk mixture and 12 μl of each molecular protein ladder (HiMark Prestained Protein Standard and Novex Sharp Prestained Protein Standard) were loaded onto either a NuPAGE 3-8% Tris-acetate or 4-12% Bis-Tris gel. Electrophoresis was conducted at a constant voltage (150V) for 55 minutes (for the 3-8% gel) or 200V for 50 minutes (for the 4-12% gel). The resulting gels were stained using a colloidal blue staining kit (ThermoFisher, Waltham, MA, USA) for 3 hours, de-stained overnight in Milli-Q water, and imaged using a ChemiDoc XRS+ gel imaging system (Bio-Rad, Hercules, CA, USA). Gel analysis was performed using Origins Gel Molecular Weight Analyzer to determine the MW of the bands observed.^[63] All SDS-PAGE consumables were sourced from ThermoFisher (Waltham, MA, USA).

Fourier Transform Infrared Spectroscopy (FTIR): Silk films were prepared for FTIR analysis by drying 2.5g of a 3% silk solution at 60 °C for 3 hours. Half of each film was immersed in

ethanol for 1 hour to induce beta-sheet crystallisation.^[6b] The films were analyzed using a Bruker LUMOS FTIR microscope (Billerica, MA, USA) equipped with a Germanium ATR crystal. Spectra were scanned over the range of 4000 – 600 cm^{-1} with a resolution of 2 cm^{-1} and 128 scans per sample. Three samples were measured for each group. Peaks corresponding to fibroin and sericin were assigned based on previous reports.^[17b, 19] Secondary structures were evaluated using the Amide I peak and the 1000 – 900 cm^{-1} in the fingerprint region,^[64] which is less influenced by water.^[64b]

Rheology: The rheological properties of the spinning dopes were measured using a Discovery Hybrid HR-1 Rheometer (TA Instruments, Newcastle, UK) equipped with a 25 mm parallel plate geometry. 20% stock solution of RSF and RUS was diluted to 15, 10, and 5%. Sufficient solution (~0.5 ml) at the desired concentration was placed on the fixed bottom plate. The top plate was lowered to 525 μm trim gap, and excess solution was gently removed before adjusting to the final gap setting of 500 μm . Prior to any measurements, a constant shear of 1 s^{-1} was applied for 100 s to eliminate residual stress from sample loading and to ensure uniform sample distribution. Flow sweep tests were performed from 0.1 s^{-1} to 200 s^{-1} over 150 s at 25 ± 1 °C and $65 \pm 2\%$ relative humidity (RH), in duplicate.

To examine mesoscale assemblies and their morphology under static and shear-induced conditions, solutions were imaged using an Olympus DP71 optical microscope (Shinjuku, Tokyo, Japan) with a $\times 20$ objective and analyzed with ImageJ (NIH, Bethesda, MD). Shear was induced by gently moving the cover slide by hand.

Wet-spinning of RSF and RUS fibers: Regenerated silk fibers were spun at RT using a laboratory-scale wet-spinning line. The spinning dope was extruded directly into a coagulation bath containing 30% (wt/v) aqueous ammonium sulphate at RT. A 1-inch 30-gauge blunt

syringe needle was positioned horizontally to the coagulation bath. A syringe pump (KDS 100 Legacy, KD Scientific, Holliston, MA, USA) was used to extrude the spinning dope at a flow rate of 2.5 ml hr^{-1} . The coagulated fiber was continuously collected on a roller at speed of 1 m min^{-1} over a period of 30 minutes. Subsequently, the collected fibers were further coagulated in the bath for 20 minutes, followed by washing with water and drying at RT. The as-spun fibers were then drawn by re-immersing them in water and extending them until twice their initial length was achieved. To induce further crystallization, the post-drawn fibers were annealed by suspending them above an open ethanol bath overnight (referred to here as post-processed fibers).

Fiber characterization: Samples were either platinum-coated or gold-coated using an EM ACE600 sputter coater (Danaher, Leica Microsystems) and imaged using a field-emission scanning electron microscope (FE-SEM, Zeiss Supra 55VP, Zeiss Leo 1530, Jeol 7800F or FEI Quanta 3D FEG) with an accelerating voltage of 2–5 kV and working distance of 5–10 mm. Fiber cross sections were obtained by fracturing perpendicular to the fiber axis under liquid nitrogen.

To assess the presence of nanofibrillar structures, samples were immersed in water at a concentration of 0.5 mg mL^{-1} and sonicated using a Qsonica Q700 sonicator (Newtown, CT, USA) equipped with a 4418 microtip probe at full power for 3 cycles of 10 minutes. Birefringence images were acquired using a Nikon Eclipse 80i polarized optical microscope (POM, Shinagawa-ku, Tokyo, Japan) with a $\times 40$ objective.

For tensile measurements, fibers were mounted onto cardboard frames using double-sided tape for positioning and superglue for fixation. Tensile strength was measured using an Agilent T150 UTM nanomechanical tensile tester (Agilent Technologies, Chandler, AZ, USA) equipped with a 50 mN load cell. Fibers with a gauge length of 10 mm were conditioned for 24 h at $21 \pm 2 \text{ }^\circ\text{C}$ and $65 \pm 2\% \text{ RH}$ prior to testing. Testing parameters included a tension trigger of $750 \mu\text{N}$,

relaxation hold time of 60 seconds, strain rate of 0.01s^{-1} , and testing at $21 \pm 2\text{ }^\circ\text{C}$ and $65 \pm 2\%$ RH.

Due to the complex morphologies of wet-spun fibers, the diameter of each fiber was calculated from SEM cross-sectional images using ImageJ (NIH, Bethesda, MD).^[64] Tensile strength, Young's modulus, tensile strain, and toughness were determined from the resultant stress-strain curves. Normality was first confirmed using a Shapiro-Wilk test, then the groups were compared with a one-way ANOVA followed by a Tukey test, with significance set at $p < 0.05$. Fiber structures were analyzed with FTIR and Raman. Prior to analysis, fibers were mounted to a glass slide covered in aluminum foil with double sided tape. FTIR was done using the same method for films. Secondary structures were evaluated by deconvoluting the amide I peak using a previously reported method,^[64a, 66] but with a deconvolution bandwidth of 34 and a noise reduction factor of 0.29. The areas under the 12 peaks were used to identify the percentage of secondary structures. Polarized Raman were obtained using an inVia microscope (Renishaw, Gloucestershire, UK) with 514 nm argon ion laser through a x50 (0.75 na) objective using a previously described method,^[67] with minor changes. Briefly, the autofluorescence of fibers was quenched by 1 hour of laser exposure. Spectra were scanned in duplicate over the range of $600 - 1800\text{ cm}^{-1}$ with a resolution of 2 cm^{-1} and 30 scans per sample. Lazer polarization was rotated using a $\frac{1}{2}$ wave plate to obtain all four polarized orientations (XX, XZ, ZX, ZZ). The crystallographic microstructure was determined through WAXS and SAXS patterns collected at the SAXS/WAXS beamline at the Australian Synchrotron (Melbourne, Australia), using a Pilatus 3-2M detector. The distance and photon energy was set to $\sim 430\text{ mm}$ and 18.1 keV for WAXS and $\sim 3200\text{mm}$ and 12keV for SAXS. Due to limited available beamtime it was not possible to record the SAXS data at fracture, and therefore estimated using the WAXS data at fracture. Data reduction was performed using XMAS (X-ray microdiffraction analysis software) and 1D peak profile fitting and instrument deconvolution was performed using Topas.

Gelation kinetics: Gelation kinetics were evaluated using a previously reported method with minor modifications.^[52a] Silk solutions at various concentrations were dispensed into covered 96-well plates. A 200 μL volume of solution was gently pipetted into each well to avoid premature shear-induced gelation. The plates were sealed with parafilm and secured with rubber bands, then incubated in a light-free environment at room temperature. Turbidity changes at 550 nm were monitored using a Varioskan LUX microplate reader (Thermo Fisher Scientific, Waltham, MA, USA). Each sample was tested in triplicate, and the results were averaged.

Fluorescent labelling: Fluorescent labelling was achieved by adding 100 μL of 10 mg ml^{-1} FITC to 900 μL of 15% RUS solution and allowing it to react overnight in darkness under ambient conditions on a roller mixer. Confocal images were obtained using a Nikon ECLIPSE Ti2 inverted confocal microscope (Minato city, Tokyo, Japan) with 405 nm and 495 nm excitation lasers and $\times 40$ objective. Identification of the fluorescing protein was conducted using SDS-PAGE as previously described but with minor adjustments. The labeled solution was prepared similarly and loaded onto a 4-12% Bis-Tris gel. Electrophoresis was carried out at a constant voltage and time of 200 V for 50 minutes. The resulting gel was imaged under trans-UV (302 nm) to visualize fluorescing bands. Subsequently, the gel was stained using a colloidal blue staining kit for 3 hours, destained overnight in Milli-Q water, and re-imaged under visible light.

SEM imaging of phase condensates: To image the phase condensates without disrupting the mesoassembly, 100 μL of 10% silk solution was sandwiched between two glass cover slides and rapidly plunged into liquid nitrogen for freeze drying. The top glass slide was carefully removed, and the sample was coated with a 3 nm layer of carbon using an EM ACE600 sputter coater (Danaher, Leica Microsystems). Subsequently, the sample was imaged using a field-

emission scanning electron microscope (FE-SEM, Zeiss Supra 55VP) at an accelerating voltage of 0.5 kV and a working distance of 2 mm.

Fiber cross-sectioning and staining: Fibers were embedded using two-part epoxy and sectioned using a steel razor blade. Sections were sanded with 4000-grit paper and polished using OP-S colloidal silica prior to staining (DYLON intense black hand dye). Sections were imaged using Nikon ECLIPSE Ti2 inverted confocal microscope (Minato city, Tokyo, Japan) with 405 nm and 640 nm excitation lasers and $\times 40$ objective.

Microencapsulation: The oil phase was prepared by dissolving Nile red in caprylic triglycerides (100 $\mu\text{g}/\text{ml}$). Then, 200 μl of the oil phase was gently added to 800 μl of 10% RUS solution. Gelation was induced by shearing the mixture using a vortex mixer. To assess dry structural stability, microcapsules were left to dry on a slide at RT. Images were captured using a $\times 20$ objective.

Foams: Foams were produced by freezing 15% silk solution in liquid nitrogen and freeze dried over two days using a Martin Christ Beta 2-8 LSC Basic Freeze Dryer (Osterode, Germany). Compression testing was done using a 5967 Instron (Norwood, MA, United States) equipped with 1kN load cell and run at 1mm min^{-1} for a maximum compressive strain of 70%. SEM images of foams was done using the same above method for fibers.

Supporting Information

Supporting Information is available from the Wiley Online Library or from the author.

Author Contributions

B.J.A. devised the project and supervised the work. M.Z. and B.J.A. conceptualized the study. M.Z. performed the experiments, analyzed the data, and took the lead in writing the manuscript with input from all authors. B.J.A., R.R., D.Y.H, and J.M.R. were involved in the planning and provided critical feedback. C.H. assisted in interpreting the results. X-ray scattering was performed by P.M. and analyzed by P.M. and P.L.

Acknowledgements

This research was supported in part by the Australian National Fabrication Facility (ANFF – Victoria). The authors acknowledge Deakin University’s Advanced Characterization Facility for the use of the Jeol 7800F, Zeiss Supra 55VP, Zeiss Leo 1530, and FEI Quanta 3D FEG FE-SEMs, as well as the valuable assistance provided by Dr Andrew Sullivan. B.J.A., R.R., and J.M.R. acknowledge support from the Australian Research Council (IH21000023). This research was partially carried out at the SAXS/WAXS beamline at the Australian Synchrotron, part of ANSTO.

Conflict of Interest Statement

Authors declare that there is no conflict of interest regarding the publication of this paper.

Data Availability Statement

The data that support the findings of this study are available from the corresponding author upon reasonable request.

Received: ((will be filled in by the editorial staff))

Revised: ((will be filled in by the editorial staff))

Published online: ((will be filled in by the editorial staff))

References

- [1] S. Blamires, *Silk: Exploring Nature's superfibre*, Xlibris Au, **2022**.
- [2] W. Qiu, A. Patil, F. Hu, X. Y. Liu, *Small* **2019**, 15, 1903948.
- [3] A. Koeppel, C. Holland, *ACS Biomaterials Science & Engineering* **2017**, 3, 226.
- [4] C. Holland, K. Numata, J. Rnjak-Kovacina, F. P. Seib, *Advanced Healthcare Materials* **2019**, 8, 1800465.
- [5] a)T. Gheysens, A. Collins, S. Raina, F. Vollrath, D. P. Knight, *Biomacromolecules* **2011**, 12, 2257; b)H. Yamada, H. Nakao, Y. Takasu, K. Tsubouchi, *Materials Science and Engineering: C* **2001**, 14, 41.
- [6] a)S. R. Koebley, D. Thorpe, P. Pang, P. Chrisochoides, I. Greving, F. Vollrath, H. C. Schniepp, *Biomacromolecules* **2015**, 16, 2796; b)B. J. Allardyce, R. Rajkhowa, R. J. Dilley, M. D. Atlas, J. Kaur, X. Wang, *Textile Research Journal* **2016**, 86, 275.
- [7] P. R. Laity, S. E. Gilks, C. Holland, *Polymer* **2015**, 67, 28.
- [8] a)S. Rastogi, B. Kandasubramanian, *The Journal of The Textile Institute* **2020**, 111, 1794; b)Y. Yao, B. J. Allardyce, R. Rajkhowa, D. Hegh, A. Sutti, S. Subianto, S. Gupta, S. Rana, S. Greenhill, S. Venkatesh, X. Wang, J. M. Razal, *ACS Biomaterials Science & Engineering* **2020**, 6, 3197; c)A. Bucciarelli, G. Greco, I. Corridori, N. M. Pugno, A. Motta, *ACS Biomaterials Science & Engineering* **2021**, 7, 1374.
- [9] J. Rnjak-Kovacina, L. S. Wray, K. A. Burke, T. Torregrosa, J. M. Golinski, W. Huang, D. L. Kaplan, *ACS Biomaterials Science & Engineering* **2015**, 1, 260.
- [10] F. Chen, D. Porter, F. Vollrath, *Acta Biomaterialia* **2012**, 8, 2620.
- [11] M. L. Gulrajani, *Review of Progress in Coloration and Related Topics* **1992**, 22, 79.
- [12] a)C. Holland, A. E. Terry, D. Porter, F. Vollrath, *Polymer* **2007**, 48, 3388; b)H. W. Kwak, J. E. Ju, M. Shin, C. Holland, K. H. Lee, *Biomacromolecules* **2017**, 18, 2343.
- [13] H.-J. Jin, D. L. Kaplan, *Nature* **2003**, 424, 1057.
- [14] H.-Y. Wang, Y.-Q. Zhang, *Soft Matter* **2013**, 9, 138.
- [15] P. R. Laity, E. Baldwin, C. Holland, *Macromolecular Bioscience* **2019**, 19, 1800188.
- [16] R. O. Moreno-Tortolero, Y. Luo, F. Parmeggiani, N. Skaer, R. Walker, L. C. Serpell, C. Holland, S. A. Davis, *Communications Biology* **2024**, 7, 786.
- [17] a)Y. Takasu, T. Hata, K. Uchino, Q. Zhang, *Insect Biochemistry and Molecular Biology* **2010**, 40, 339; b)J. Sparkes, C. Holland, *Acta Biomaterialia* **2018**, 69, 234; c)A. Garel, G. Deleage, J.-C. Prudhomme, *Insect Biochemistry and Molecular Biology* **1997**, 27, 469; d)T. Da Silva, A. Junior, M. Ribani, M. Vieira, M. Gimenes, M. Da Silva, *Chemical Engineering Transactions* **2014**, 38, 103.

- [18] a)J.-J. Max, C. Chapados, *The Journal of Physical Chemistry A* **2004**, 108, 3324; b)A. Percot, P. Colombari, C. Paris, H. M. Dinh, M. Wojcieszak, B. Mauchamp, *Vibrational Spectroscopy* **2014**, 73, 79.
- [19] X. Zhang, P. Wyeth, *Science China Chemistry* **2010**, 53, 626.
- [20] C. Holland, N. Hawkins, M. Frydrych, P. Laity, D. Porter, F. Vollrath, *Macromolecular Bioscience* **2019**, 19, 1800228.
- [21] R. M. Daniel, M. Dines, H. H. Petach, *Biochem J* **1996**, 317 (Pt 1), 1.
- [22] R. Kol, P. Nachtergaele, T. De Somer, D. R. D'hooge, D. S. Achilias, S. De Meester, *Industrial & Engineering Chemistry Research* **2022**, 61, 10999.
- [23] R. Pal, *Journal of Rheology - J RHEOL* **2001**, 45, 509.
- [24] a)A. Leppert, G. Chen, D. Lama, C. Sahin, V. Railaite, O. Shilkova, T. Arndt, E. G. Marklund, D. P. Lane, A. Rising, M. Landreh, *Nano Letters* **2023**, 23, 5836; b)C. Schaefer, P. R. Laity, C. Holland, T. C. B. McLeish, *Macromolecules* **2020**, 53, 2669; c)C. Schaefer, P. R. Laity, C. Holland, T. C. B. McLeish, *Molecules* **2021**, 26, 1663; d)C. Schaefer, T. C. B. McLeish, *Journal of Rheology* **2022**, 66, 515.
- [25] a)L. D. Muiznieks, J. T. Cirulis, A. van der Horst, D. P. Reinhardt, G. J. L. Wuite, R. Pomès, F. W. Keeley, *Matrix Biology* **2014**, 36, 39; b)S. Elbaum-Garfinkle, Y. Kim, K. Szczepaniak, C. C.-H. Chen, C. R. Eckmann, S. Myong, C. P. Brangwynne, *Proceedings of the National Academy of Sciences* **2015**, 112, 7189.
- [26] L. Lemetti, S.-P. Hirvonen, D. Fedorov, P. Batys, M. Sammalkorpi, H. Tenhu, M. B. Linder, A. S. Aranko, *European Polymer Journal* **2019**, 112, 539.
- [27] a)H.-J. Jin, J. Park, R. Valluzzi, P. Cebe, D. L. Kaplan, *Biomacromolecules* **2004**, 5, 711; b)X. Wang, Z. Ding, C. Wang, X. Chen, H. Xu, Q. Lu, D. L. Kaplan, *J Mater Chem B* **2018**, 6, 2739.
- [28] a)A. D. Malay, T. Suzuki, T. Katashima, N. Kono, K. Arakawa, K. Numata, *Science Advances* **2020**, 6, eabb6030; b)E. Astoricchio, C. Alfano, L. Rajendran, P. A. Temussi, A. Pastore, *Trends in Biochemical Sciences* **2020**, 45, 706.
- [29] a)P. Kudella, K. Preißinger, M. Morasch, C. Dirscherl, D. Braun, A. Wixforth, C. Westerhausen, *Scientific Reports* **2019**, 9, 18808; b)P. Mohammadi, A. S. Aranko, L. Lemetti, Z. Cenev, Q. Zhou, S. Virtanen, C. P. Landowski, M. Penttilä, W. J. Fischer, W. Wagermaier, M. B. Linder, *Communications Biology* **2018**, 1, 86; c)Y. Shen, F. S. Ruggeri, D. Vigolo, A. Kamada, S. Qamar, A. Levin, C. Iserman, S. Alberti, P. S. George-Hyslop, T. P. J. Knowles, *Nat Nanotechnol* **2020**, 15, 841.

- [30] a)K. Yazawa, K. Nakayama, Y. Gotoh, *ACS Sustainable Chemistry & Engineering* **2023**, 11, 2151; b)J. Yan, G. Zhou, D. P. Knight, Z. Shao, X. Chen, *Biomacromolecules* **2010**, 11, 1.
- [31] S.-W. Ha, A. E. Tonelli, S. M. Hudson, *Biomacromolecules* **2005**, 6, 1722.
- [32] D. Perera, L. Li, C. Walsh, Q. Wang, H. C. Schniepp, **2022**.
- [33] H. Lu, K. Xia, M. Jian, X. Liang, Z. Yin, M. Zhang, H. Wang, H. Wang, S. Li, Y. Zhang, *Research* **2022**, 2022.
- [34] M. McGill, G. P. Holland, D. L. Kaplan, *Macromolecular Rapid Communications* **2019**, 40, 1800390.
- [35] A. Nova, S. Keten, N. M. Pugno, A. Redaelli, M. J. Buehler, *Nano Lett* **2010**, 10, 2626.
- [36] a)S. Keten, Z. Xu, B. Ihle, M. J. Buehler, *Nature Materials* **2010**, 9, 359; b)T. Giesa, M. Arslan, N. M. Pugno, M. J. Buehler, *Nano Letters* **2011**, 11, 5038.
- [37] H. Zhang, W. Liu, Y. Ding, F. Tian, Z. Tang, *Polymer Testing* **2021**, 99, 107218.
- [38] H. Masunaga, H. Ogawa, T. Takano, S. Sasaki, S. Goto, T. Tanaka, T. Seike, S. Takahashi, K. Takeshita, N. Nariyama, H. Ohashi, T. Ohata, Y. Furukawa, T. Matsushita, Y. Ishizawa, N. Yagi, M. Takata, H. Kitamura, K. Sakurai, K. Tashiro, A. Takahara, Y. Amamiya, K. Horie, M. Takenaka, T. Kanaya, H. Jinnai, H. Okuda, I. Akiba, I. Takahashi, K. Yamamoto, M. Hikosaka, S. Sakurai, Y. Shinohara, A. Okada, Y. Sugihara, *Polymer Journal* **2011**, 43, 471.
- [39] Y. Yao, B. J. Allardyce, R. Rajkhowa, C. Guo, X. Mu, D. Hegh, J. Zhang, P. Lynch, X. Wang, D. L. Kaplan, J. M. Razal, *Biomacromolecules* **2021**, 22, 788.
- [40] a)T. Chaiyaso, P. Rachtanapun, N. Thajai, K. Kiattipornpithak, P. Jantrawut, W. Ruksiriwanich, P. Seesuriyachan, N. Leksawasdi, Y. Phimolsiripol, C. Techapun, S. R. Sommano, T. Ougizawa, K. Yakul, K. Jantanasakulwong, *Scientific Reports* **2021**, 11, 19945; b)P. S. Garcia, F. R. B. Turbiani, A. M. Baron, G. L. Brizola, M. A. Tavares, F. Yamashita, D. Eiras, M. V. E. Grossmann, *Polímeros* **2018**, 28.
- [41] B. Ode Boni, B. Bakadia, A. Osi, Z. Shi, H. Chen, M. Gauthier, G. Yang, *Macromolecular bioscience* **2021**, 22, e2100292.
- [42] C. Ye, L. Cao, S. Ling, in *Fibrous Proteins: Design, Synthesis, and Assembly*, (Ed: S. Ling), Springer US, New York, NY 2021.
- [43] R. P. Burford, D. R. G. Williams, *Journal of Materials Science* **1979**, 14, 2872.
- [44] R. Rajkhowa, J. Kaur, X. Wang, W. Batchelor, *Journal of The Royal Society Interface* **2015**, 12, 20150177.

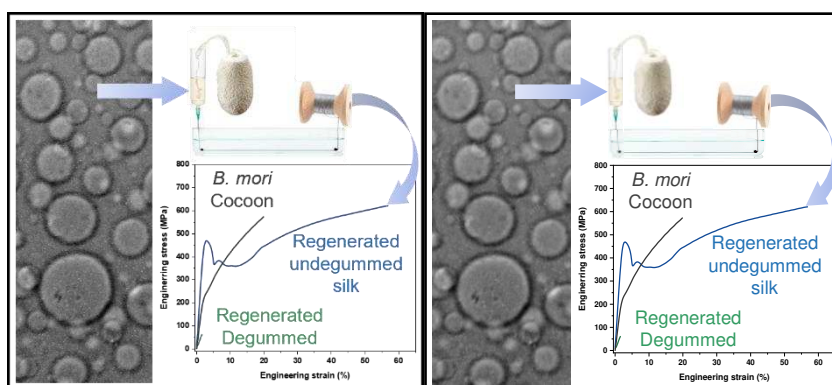
- [45] B. Mortimer, J. Guan, C. Holland, D. Porter, F. Vollrath, *Acta Biomaterialia* **2015**, *11*, 247.
- [46] a)C. Sauder, J. Lamon, *Carbon* 2005, *43*, 2044; b)M. G. Northolt, L. H. Veldhuizen, H. Jansen, *Carbon* 1991, *29*, 1267.
- [47] a)Q. Wan, N. T. H. Farr, P. Li, D. Batey, C. Rau, J. Rodenburg, L. Lu, P. R. Laity, Z. Xu, C. Holland, C. Rodenburg, M. Yang, *Small Structures* 2024, *5*, 2300435; b)Q. Wan, M. Yang, J. Hu, F. Lei, Y. Shuai, J. Wang, C. Holland, C. Rodenburg, M. Yang, *Nature Communications* 2021, *12*, 3711.
- [48] N. Du, Z. Yang, X. Y. Liu, Y. Li, H. Y. Xu, *Advanced Functional Materials* 2011, *21*, 772.
- [49] L. Fan, J.-L. Li, Z. Cai, X. Wang, *Nature Communications* 2021, *12*, 2375.
- [50] a)Y. Yao, B. J. Allardyce, R. Rajkhowa, D. Hegh, S. Qin, K. A. S. Usman, P. Mota-Santiago, J. Zhang, P. Lynch, X. Wang, D. L. Kaplan, J. M. Razal, *Macromolecular Rapid Communications* 2022, *43*, 2100891; b)J. Wang, T. Fan, X. Li, X. Hu, W. Huang, W. Yuan, Z. Lin, *Matter* 2022, *5*, 4396.
- [51] a)D. Eliaz, S. Paul, D. Benyamin, A. Cernescu, S. R. Cohen, I. Rosenhek-Goldian, O. Brookstein, M. E. Miali, A. Solomonov, M. Greenblatt, Y. Levy, U. Raviv, A. Barth, U. Shimanovich, *Nature Communications* 2022, *13*, 7856; b)A. D. Malay, H. C. Craig, J. Chen, N. A. Oktaviani, K. Numata, *Biomacromolecules* 2022, *23*, 1827.
- [52] a)A. Matsumoto, J. Chen, A. L. Collette, U.-J. Kim, G. H. Altman, P. Cebe, D. L. Kaplan, *The Journal of Physical Chemistry B* 2006, *110*, 21630; b)U. J. Kim, J. Park, C. Li, H. J. Jin, R. Valluzzi, D. L. Kaplan, *Biomacromolecules* 2004, *5*, 786.
- [53] G. J. Dunderdale, S. J. Davidson, A. J. Ryan, O. O. Mykhaylyk, *Nature Communications* 2020, *11*, 3372.
- [54] S. Park, R. Barnes, Y. Lin, B.-j. Jeon, S. Najafi, K. T. Delaney, G. H. Fredrickson, J.-E. Shea, D. S. Hwang, S. Han, *Communications Chemistry* 2020, *3*, 83.
- [55] C.-I. Ren, R. J. Nap, I. Szleifer, *The Journal of Physical Chemistry B* 2008, *112*, 16238.
- [56] L. Lemetti, A. Scacchi, Y. Yin, M. Shen, M. B. Linder, M. Sammalkorpi, A. S. Aranko, *Biomacromolecules* 2022, *23*, 3142.
- [57] a)K. Yamaguchi, Y. Kikuchi, T. Takagi, A. Kikuchi, F. Oyama, K. Shimura, S. Mizuno, *Journal of Molecular Biology* 1989, *210*, 127; b)S. Inoue, K. Tanaka, F. Arisaka, S. Kimura, K. Ohtomo, S. Mizuno, *Journal of Biological Chemistry* 2000, *275*, 40517.
- [58] G. Esposito, Y. Dimakopoulos, J. Tsamopoulos, *Journal of Non-Newtonian Fluid Mechanics* 2023, *321*, 105124.

- [59] M. Zaki, Great Britain Patent WO2023285609.
- [60] a)S. Miyake, M. Azuma, *Journal of Insect Biotechnology and Sericology* 2008, 77, 9;
b)L. J. Domigan, M. Andersson, K. A. Alberti, M. Chesler, Q. Xu, J. Johansson, A. Rising, D. L. Kaplan, *Insect Biochem Mol Biol* 2015, 65, 100.
- [61] a)L. Zhou, X. Chen, Z. Shao, Y. Huang, D. P. Knight, *The Journal of Physical Chemistry B* 2005, 109, 16937; b)L. Zhou, X. Chen, Z. Shao, P. Zhou, D. P. Knight, F. Vollrath, *FEBS Lett* 2003, 554, 337; c)A. Koepfel, P. R. Laity, C. Holland, *Acta Biomaterialia* 2020, 117, 204.
- [62] J. Sparkes, C. Holland, *Nature Communications* 2017, 8, 594.
- [63] Origin, Vol. 2019b, Origin, 2019.
- [64] a)X. Hu, D. Kaplan, P. Cebe, *Macromolecules* 2006, 39, 6161; b)T. Yoshioka, K. Tashiro, N. Ohta, *Biomacromolecules* 2016, 17, 1437.
- [65] G. Greco, B. Schmuck, S. K. Jalali, N. M. Pugno, A. Rising, *Biophysics Reviews* 2023, 4.
- [66] M. G. Uddin, B. J. Allardyce, N. Rashida, R. Rajkhowa, *International Journal of Biological Macromolecules* 2021, 179, 20.
- [67] J. Poole, J. S. Church, A. L. Woodhead, M. G. Huson, A. Sriskantha, I. L. Kyratzis, T. D. Sutherland, *Macromolecular Bioscience* 2013, 13, 1321

Dissolving Undegummed silk leads to a solution with undegraded silk that exhibits liquid-liquid phase separation (LLPS). Spinning the solution leads to fibers with a ~20nm nanofibrillar hierarchy that are 2.3 times tougher than natural silk fibers. This establishes the importance of retaining molecular weight, presence of sericins, and priming LLPS in designing tougher-than-nature fibers with fibrillar hierarchy.

M. Zaki, R. Rajkhowa, C. Holland, J. M. Razal, D. Y. Hegh, P. Mota-Santiago, P. Lynch, B. J. Allardyce

Recreating Silk's Fibrillar Nanostructure by Spinning Solubilized, Undegummed Silk



Supporting Information

Recreating Silk's Fibrillar Nanostructure by Spinning Solubilized, Undegummed Silk

Martin Zaki, Rangam Rajkhowa, Chris Holland, Joselito Macabuhay Razal, Dylan Yalmar Hegh, Pablo Mota-Santiago, Peter Lynch, Benjamin James Allardyce*

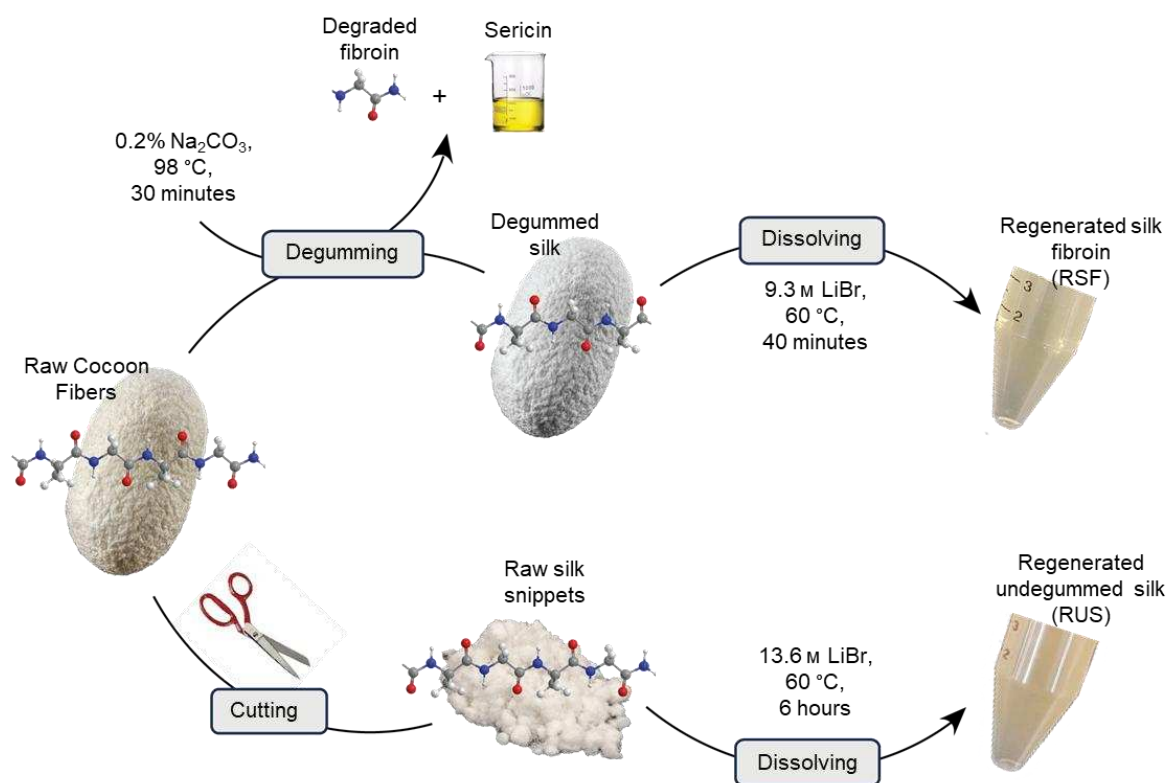


Figure S1. Schematic of the two dissolution methods. Typical RSF is prepared by Na₂CO₃ degumming followed by LiBr dissolution,^[1] while RUS is prepared by cutting fibers into snippets, followed by dissolution in super-saturated LiBr.

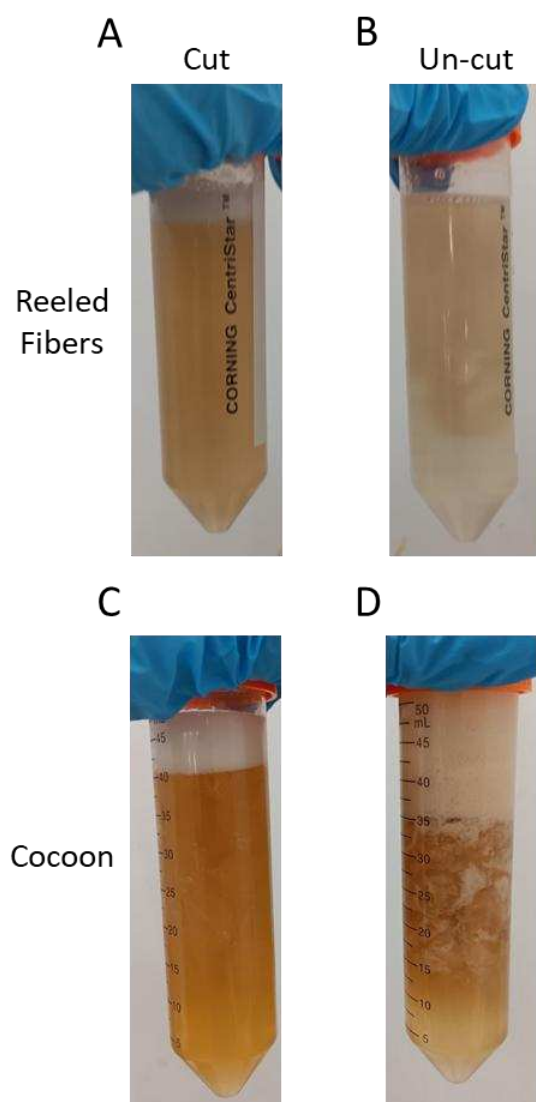


Figure S2. RUS dissolution using cut and un-cut silk. Prerequisite cutting is a required to produce a homogeneous solution (A and C), while un-cut silk leads to incomplete dissolution (B and D).

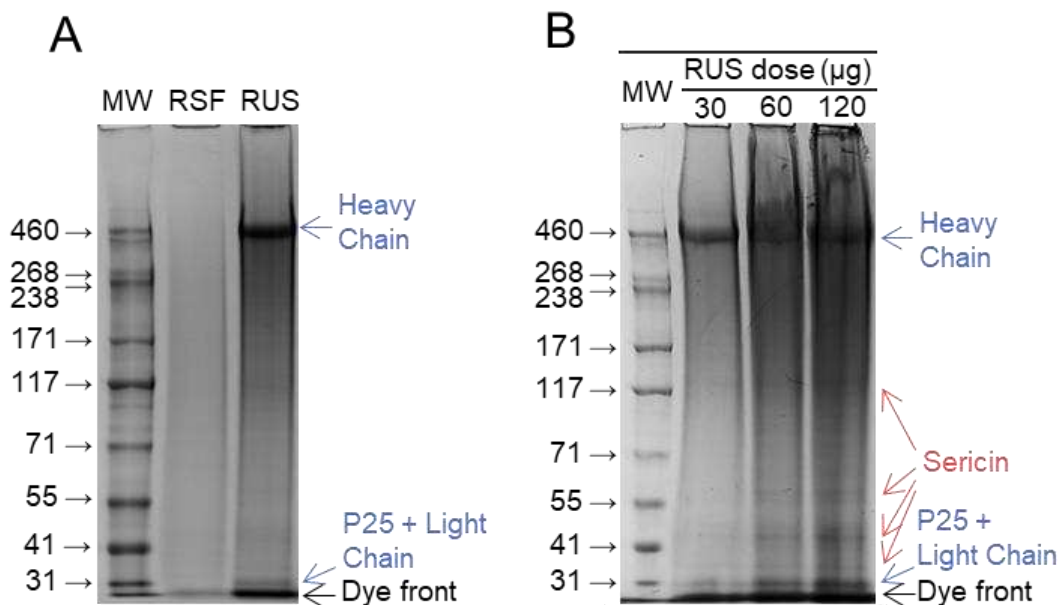


Figure S3. MW analysis of RSF and RUS using A) a 3-8% gel and B) RUS at 30, 60 and 120 μg loading. RSF processing leads to hydrolysis of the heavy chain and the removal of the P25 and light chain.^[2] On the other hand, RUS shows minor smearing at higher MWs with the SDS-PAGE analogous to reported gland silk.^[3] Overloading PAGEs with protein can lead to protein aggregation, affecting protein migration and causing artefactual zones in the high molecular weight area (> 500 kDa) as well as vertical streaking.^[4] Therefore, the 30 μg loaded sample is considered most representative of the actual protein MWs in the sample.

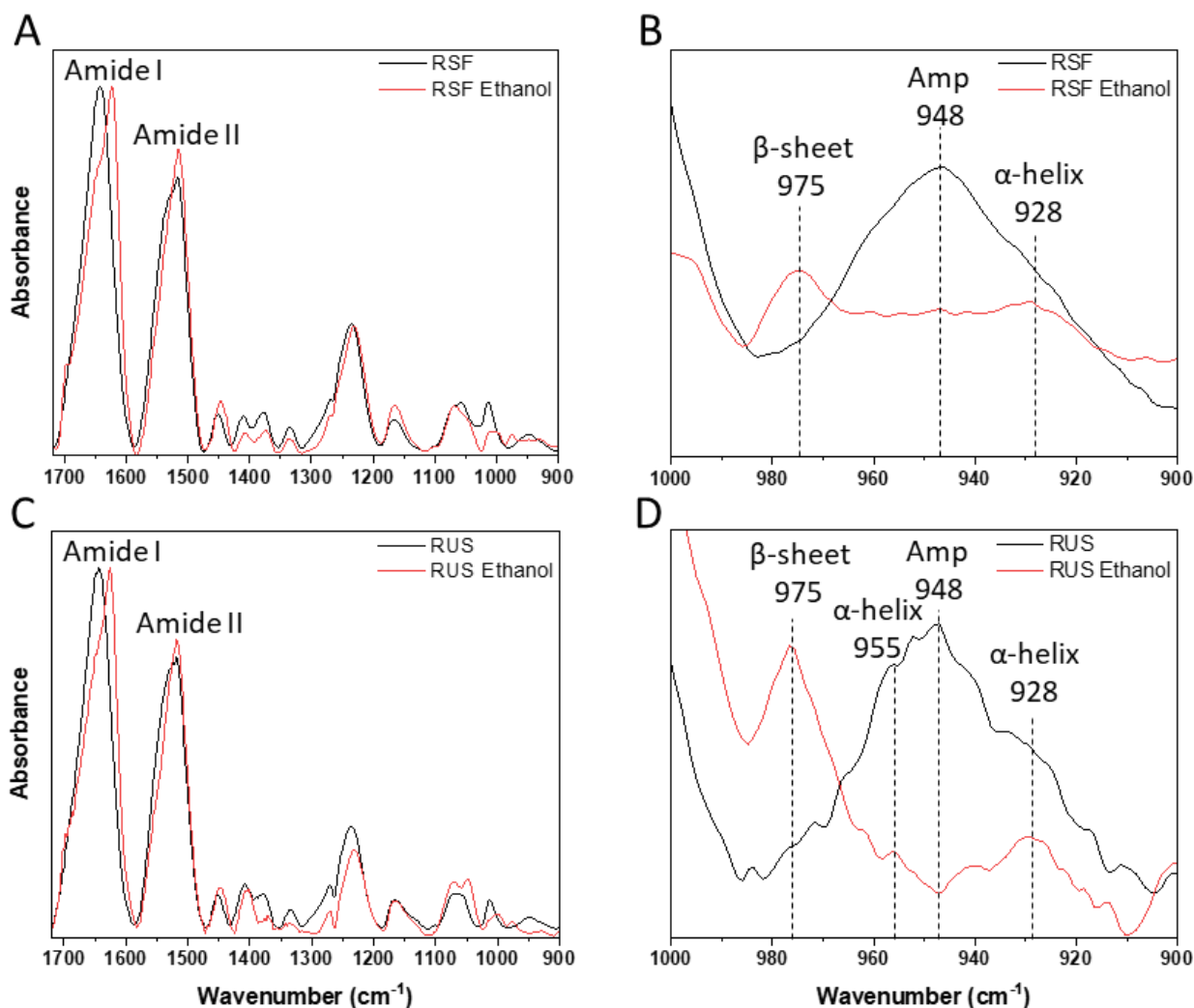


Figure S4. FTIR spectra of RSF and RUS films before and after ethanol treatment. When analyzing the conventional Amide I and Amide II peaks, RSF and RUS appear very similar before and after ethanol treatment. A shift towards lower frequencies is observed with ethanol treatment associated with the development of β -sheets. However, further examination at $1000 - 900 \text{ cm}^{-1}$ reveals differences in the secondary structures,^[5] with RUS abundant in α -helices and RSF rich in amorphous structures.

Identifying sericin within RUS fibers

Staining is sometimes used to differentiate between sericin and fibroin. In general dyes preferentially stain to sericin.^[6] When the cocoon baves were imaged optically, the dye was found to preferentially stain the sericin. By using the cocoon baves as a standard, the two most contrasting laser excitation wavelengths were identified. 405nm can excite auto-fluorescing proteins, while 640nm was identified to excite the dye within the sericin. However, the dye was found to indiscriminately stain RUS and RSF even though sericin is not present in RSF (**Figure S5**). The dye used in our method likely binds according to porosity, leading to poor staining in the dense cocoon brins but allows for staining in the regenerated fibers.

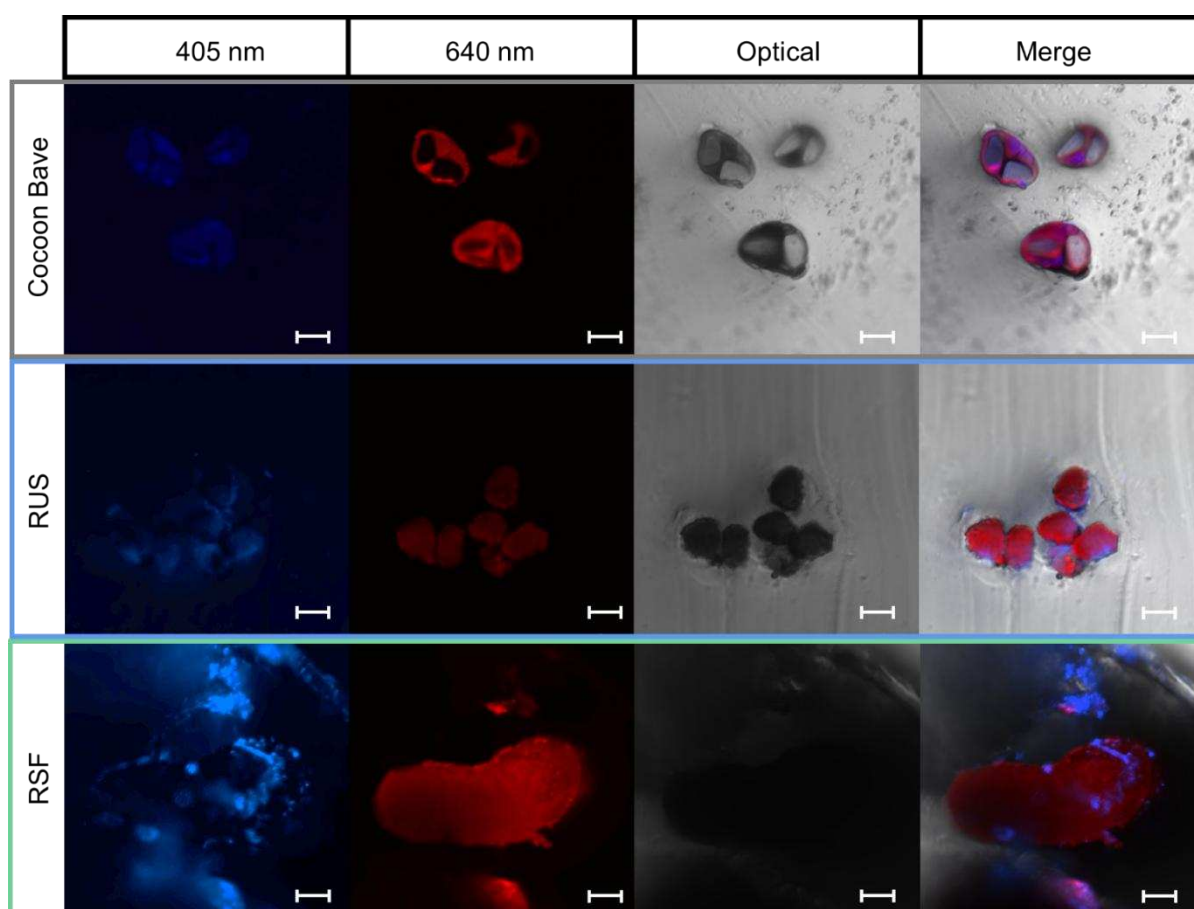


Figure S5. Confocal images of cross-sectioned fibers, with excitation at 405 nm to visualize auto-fluorescing proteins, at 640 nm to visualize the dye, the optical image, and the merged images of the three. Scale bar: 10 μ m

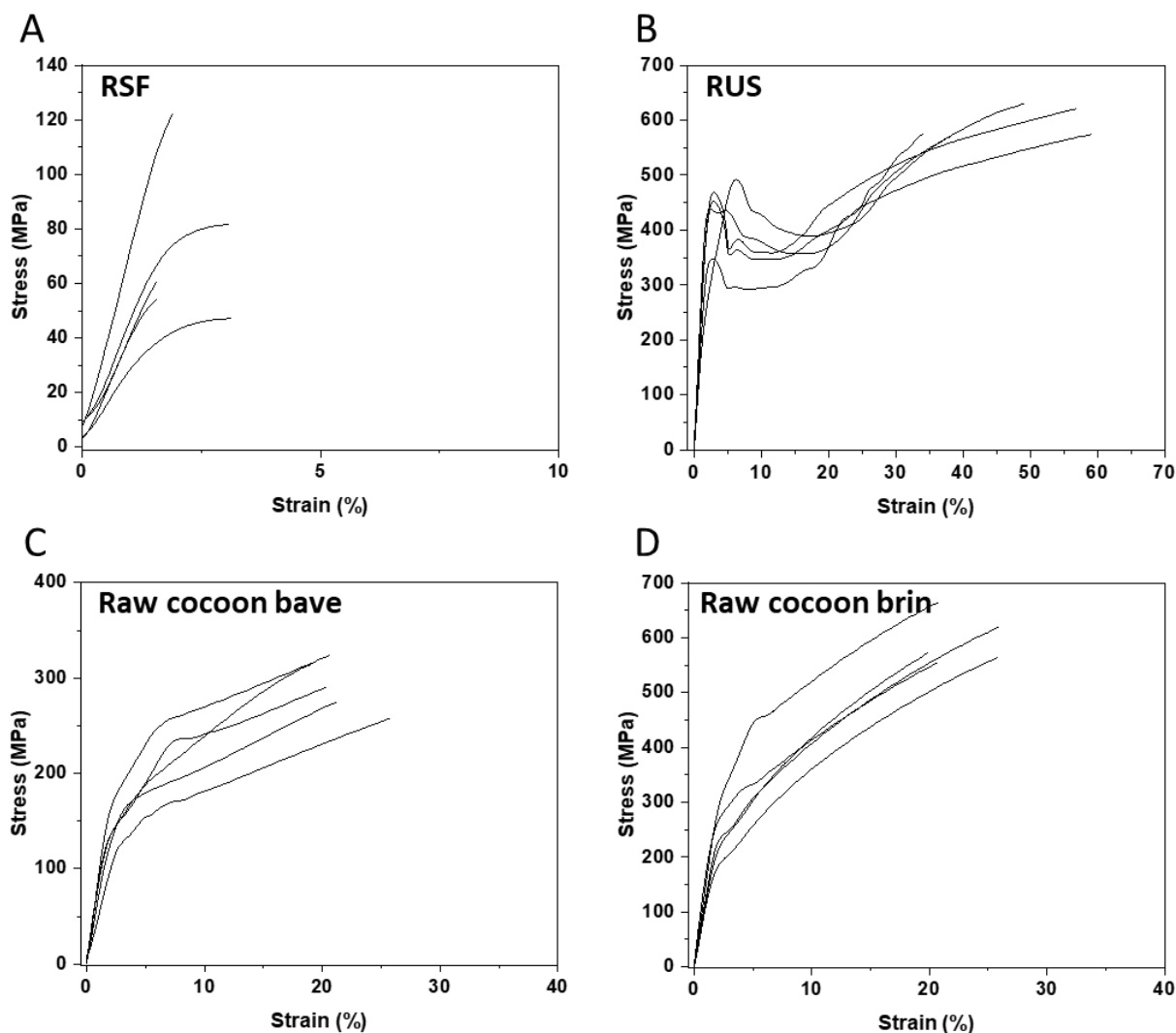


Figure S6. Tensile stress-strain curves of RSF, RUS and cocoon fibers. RSF, bave, and brin stress-strain curves and their mechanical properties match previous results.^[7] However, RUS had a stress-strain profile resembling minor ampullate spider silk.^[8]

Table S1. Mechanical properties obtained from fiber stress-strain curves (\pm SD).

Fiber	Diameter [μ m]	Youngs modulus [GPa]	Engineering Strain [%]	Engineering Stress [MPa]	Toughness [MJm ⁻³]
Baves	15.1 [\pm 2.3]	7.75 [\pm 1.7]	21.32 [\pm 2.6]	291.83 [\pm 27.4]	45.98 [\pm 4.0]
Brins	10.9 [\pm 1.3]	13.44 [\pm 2.8]	22.98 [\pm 3.2]	576.61 [\pm 29.0]	92.23 [\pm 15.4]
RSF	29.3 [\pm 8.2]	4.57 [\pm 1.6]	2.22 [\pm 0.7]	73.01 [\pm 30.3]	0.98 [\pm 0.5]
RUS	16.6 [\pm 4.2]	22.84 [\pm 3.6]	47.36 [\pm 11.0]	594.17 [\pm 28.5]	213.03 [\pm 65.9]

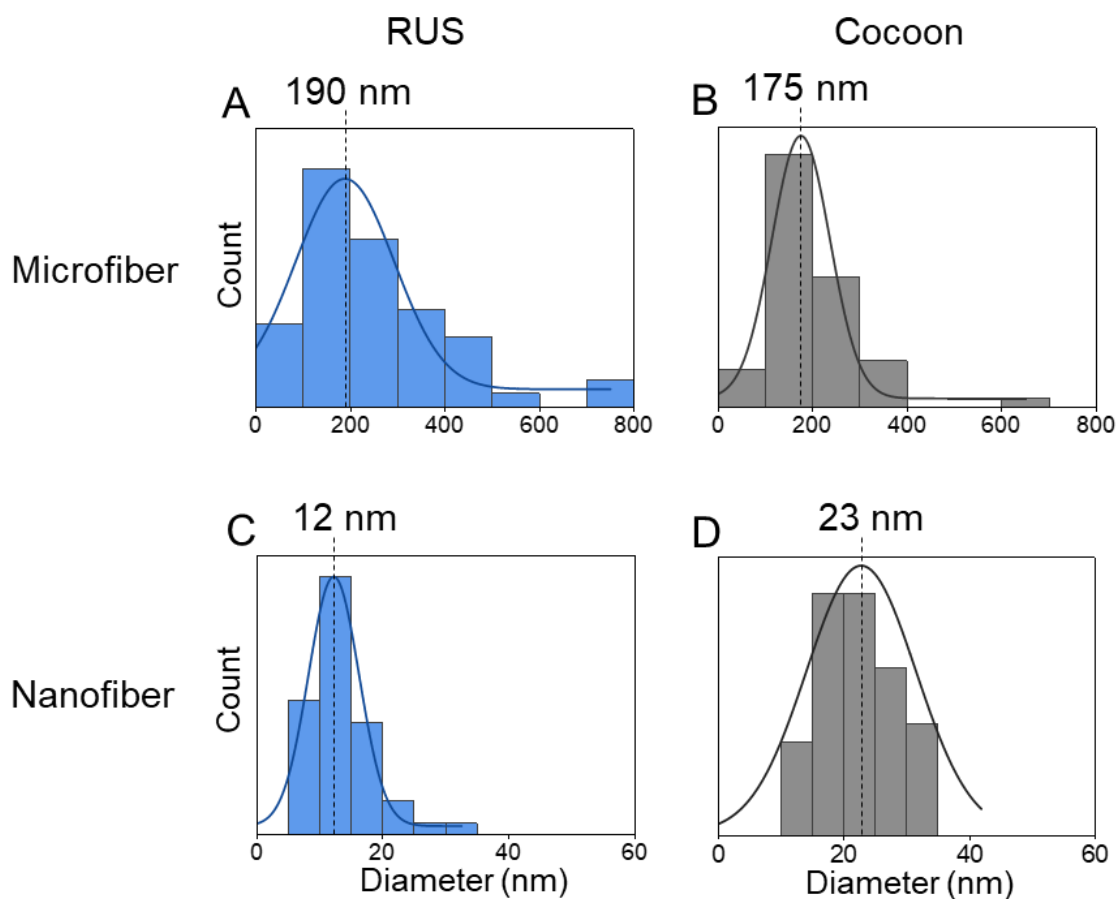


Figure S7. Diameter distribution of microfibrils (A and B) and nanofibrils (C and D) exposed via sonication. Cocoon microfibrils were measured from sonicated fibers and nanofibrils from the sonicated supernatant. Although the average microfibril diameters are similar, polydispersity is greater in RUS. Cocoon nanofibrils are twice the diameter of RUS. $n=50$ and dashed line is the mode.

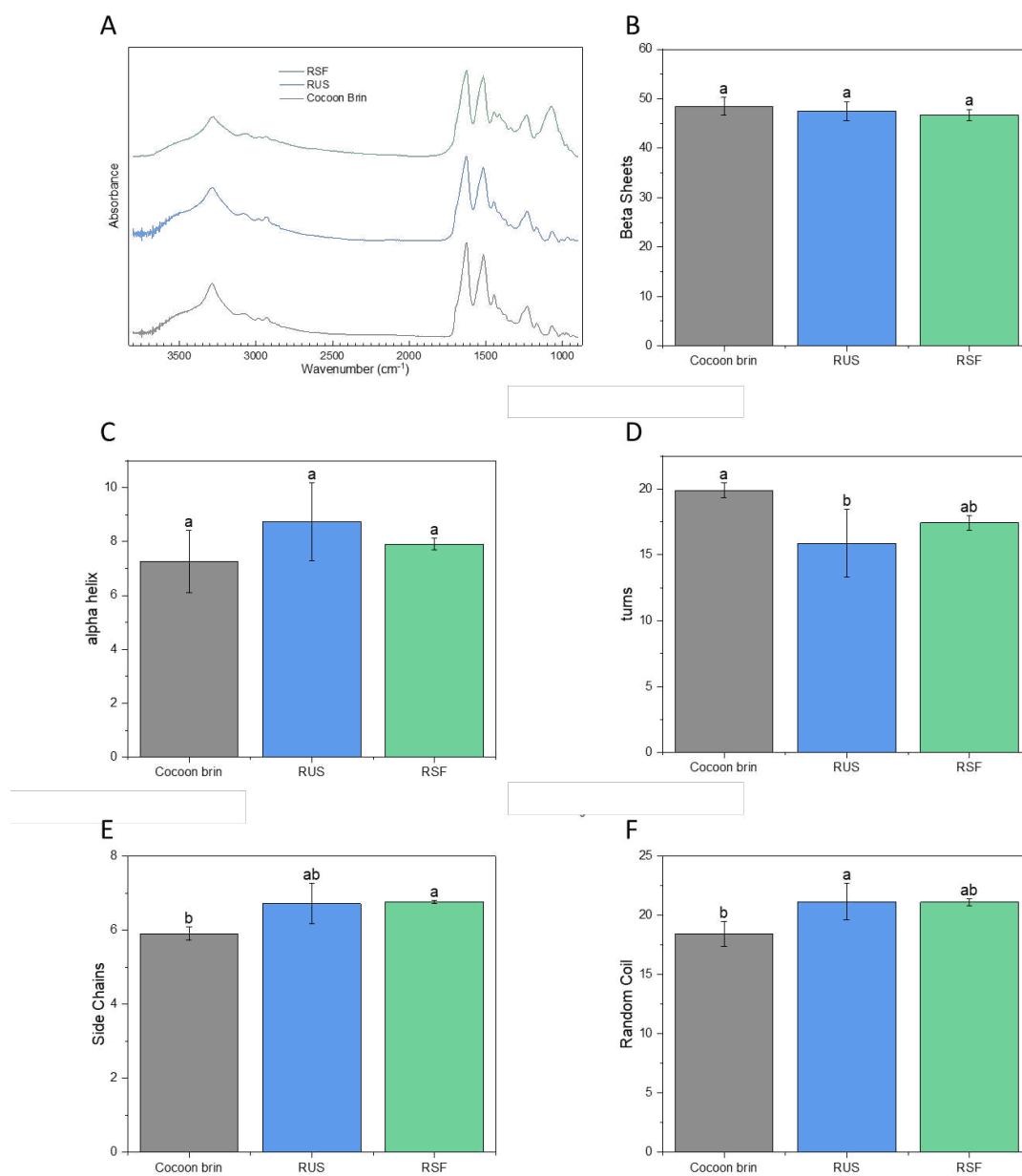


Figure S8. FTIR analysis of the different fibers. A) The full spectra alongside the average proportions of secondary structures calculated from deconvoluting the Amide I peak (B to F). $n=3$, error bars = SD, results are normally distributed (Shapiro-Wilk), and groups are significantly different (Tukey, $p<0.05$).

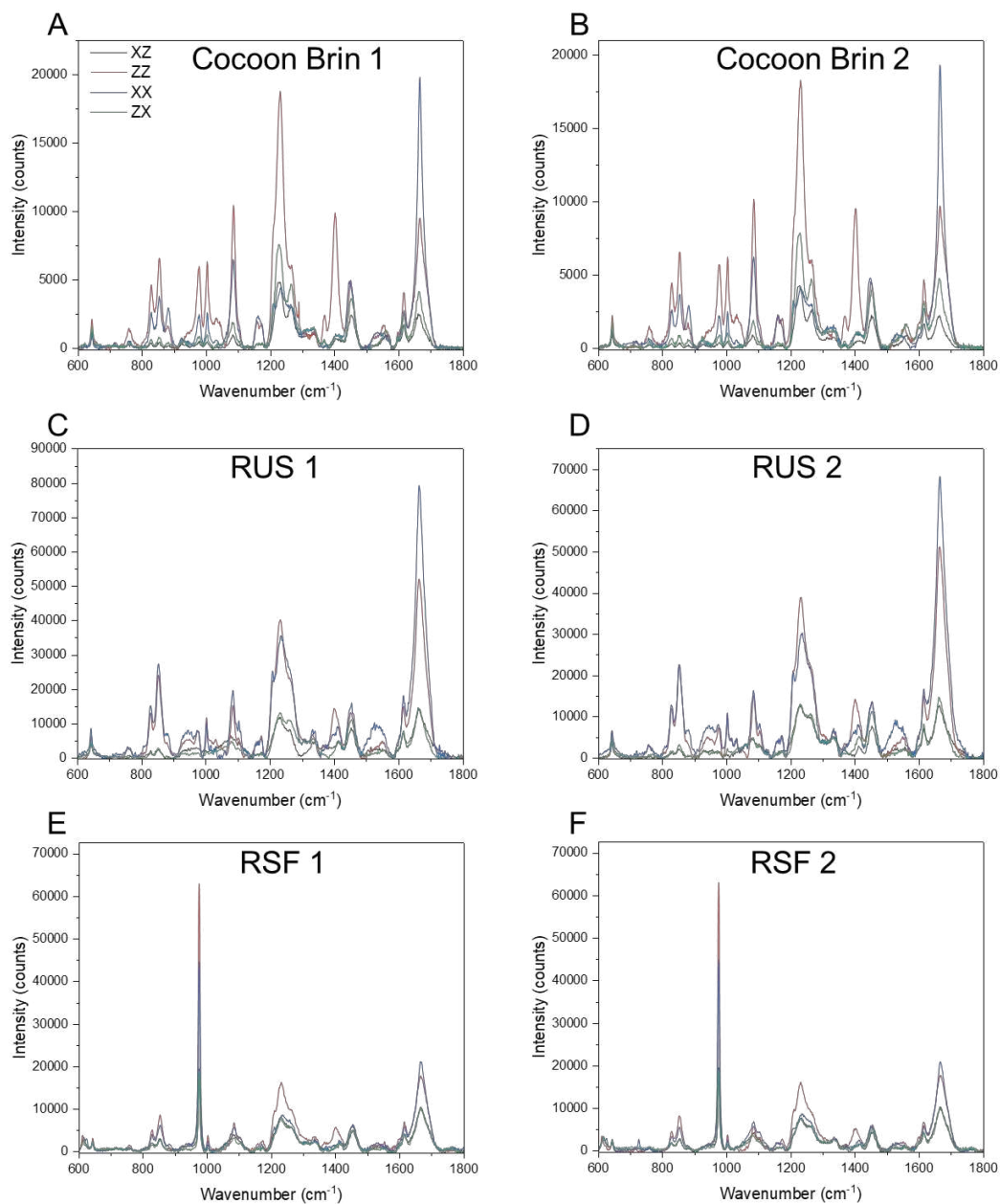


Figure S9. Polarized Raman spectra obtained from Cocoon brins (A and B), RUS (C and D), and RSF (E and F).

WAXS calculation of Herman's orientation factor and crystallite size

Orientation factor (f) was calculated by azimuthal integration of the (020) reflection from the WAXS 2D pattern and numerically fitted according to Herman's orientation function (Equation S1)

$$f = \frac{3 \langle \cos^2 \Phi \rangle - 1}{2} \quad (\text{S1})$$

Where ϕ corresponds to the angle between the c-axis and the fiber axis is defined as

$$\langle \cos^2 \Phi \rangle = \frac{\int_0^{\pi/2} I(\Phi) \cos^2 \Phi \sin \Phi d\Phi}{\int_0^{\pi/2} I(\Phi) \sin \Phi d\Phi} \quad (\text{S2})$$

As a result, a value of $f = 1$ corresponds to crystals perfectly aligned along the fiber axis. In contrast, when $f = 0$ crystals are randomly oriented, readily observed in the raw 2D data as isotropic scattering.

The crystallite size (L) was calculated using Sherrer equation S3 after the instrumental contribution was deconvoluted from raw data using a previously described method.^[9]

$$L = \frac{0.9\lambda}{\text{FWHM} \cos \Phi} \quad (\text{S3})$$

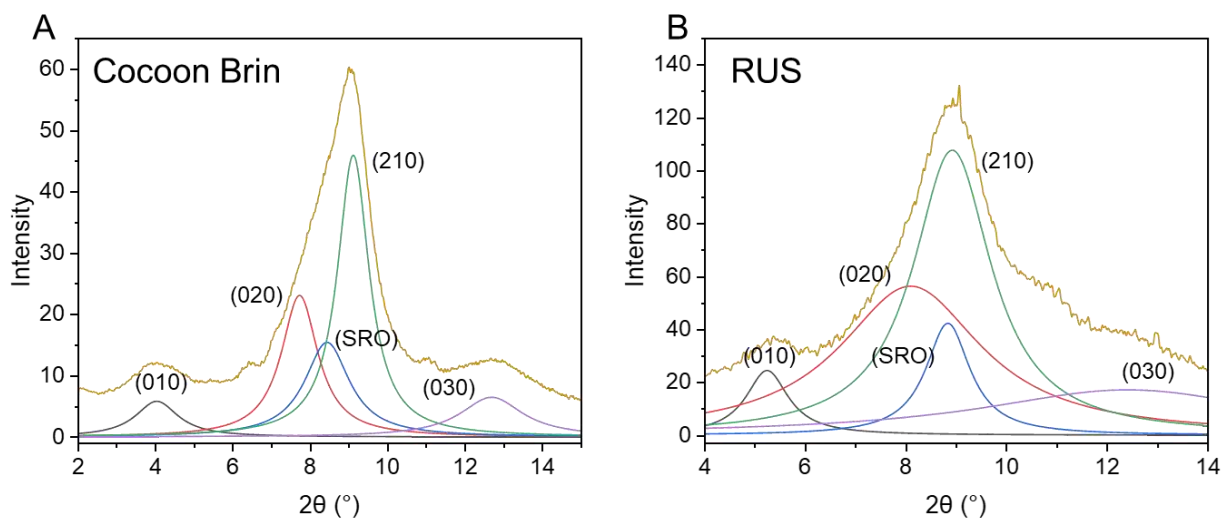


Figure S10. Peak deconvolution of 1D equatorial plots of A) cocoon brin and B) RUS fibers.

Table S2. Azimuthal angle, $\text{Cos}^2\Phi$, Orientation factor and crystallite size calculated from the 2D WAXS patterns. Where crystallite size = \pm SD.

Sample	Azimuthal angle Ψ (°)	$\text{Cos}^2\Phi$	Orientation factor f	Crystallite size L (nm)
Cocoon brin	18.04	0.98	0.97	3.43 (\pm 0.27)
RSF	N/A (isotropic)	N/A	0	24.38 (\pm 0.27)
RUS	40.1	0.89	0.84	1.16 (\pm 0.20)
RUS 20%	38.05	0.91	0.86	1.36 (\pm 0.11)
RUS fractured	31.28	0.93	0.89	1.49 (\pm 0.15)

SAXS calculation of orientation index and Ruland's approach

The SAXS pattern is comprised by a characteristic ellipsoid pattern along the equatorial direction, related to the presence of voids. The width of the scattering pattern can be related to the preferential orientation by fitting azimuthal scans with increasing q -values.^[10]

Once the breadth of each scattering intensity is determined, the length and misorientation can be determined using Ruland's function:

$$q^2 B_{obs}^2 = \frac{1}{L^2} + q^2 B_g^2 \quad (S5)$$

Where B_{obs} corresponds to the orientation distribution as determined from the measurement, L is the average void length and B_g is the orientation distribution in real space.

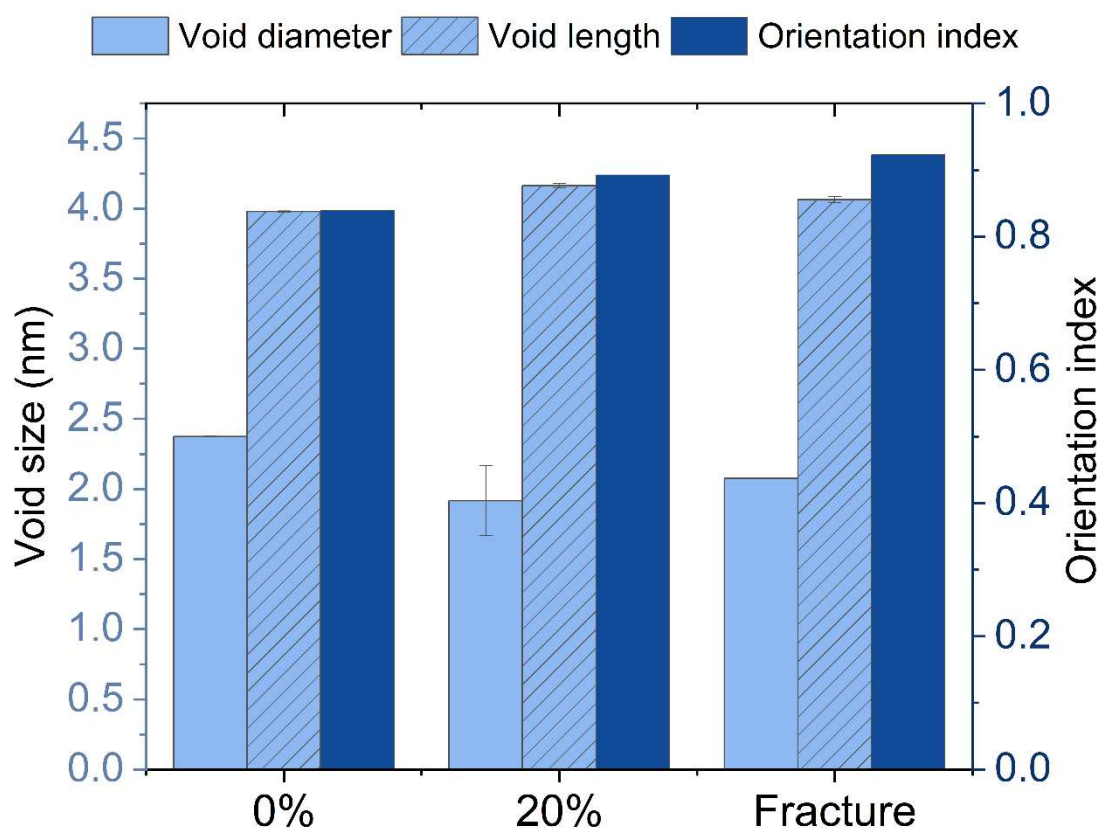


Figure S11. Void diameter, length and orientation calculated using Ruland's approach on SAXS patterns.

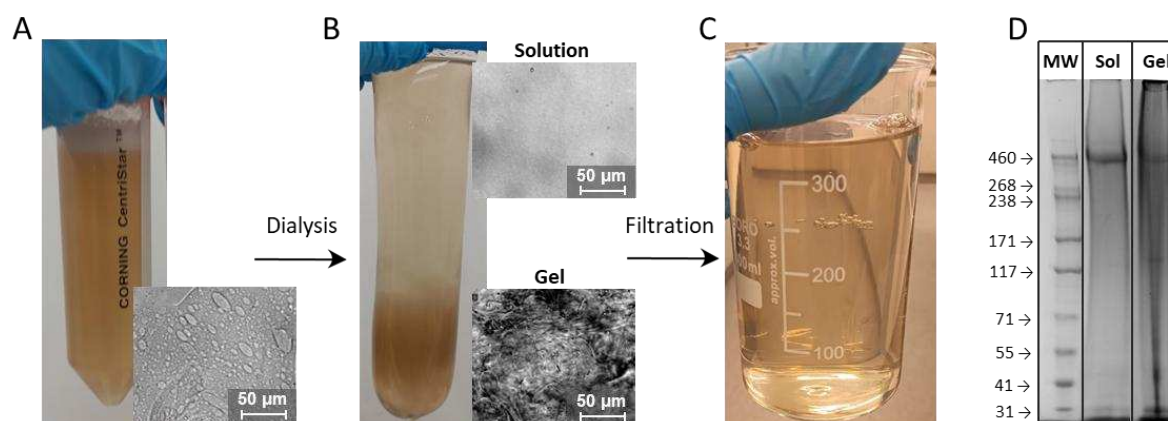


Figure S12. Analysis of incomplete dissolution. A) Before dialysis, a homogenous solution is obtained. Although no undissolved fibers are present, surprisingly, phase separation is observed. This is likely due to salt induced dehydration of the saturated LiBr, which has been previously observed with other salts.^[11] B) After dialysis, two phases are clearly observed; solution (top) and a gel (bottom). The solution lacks any phase condensates. On the other hand, the gel appears to consist of micro- and nano-fibers. As fibers are not present before dialysis but present after dialysis, it is likely that the fibers are formed as an artefact of dialysis. C) After filtration, the solution is clear and has a yellow tint analogous to silk solutions. To compare the difference between the two phases a D) 3-8% SDS-PAGE was run. Identical bands were observed with streaking present in the gel lane due to incomplete dissolution prior to electrophoresis.^[4]

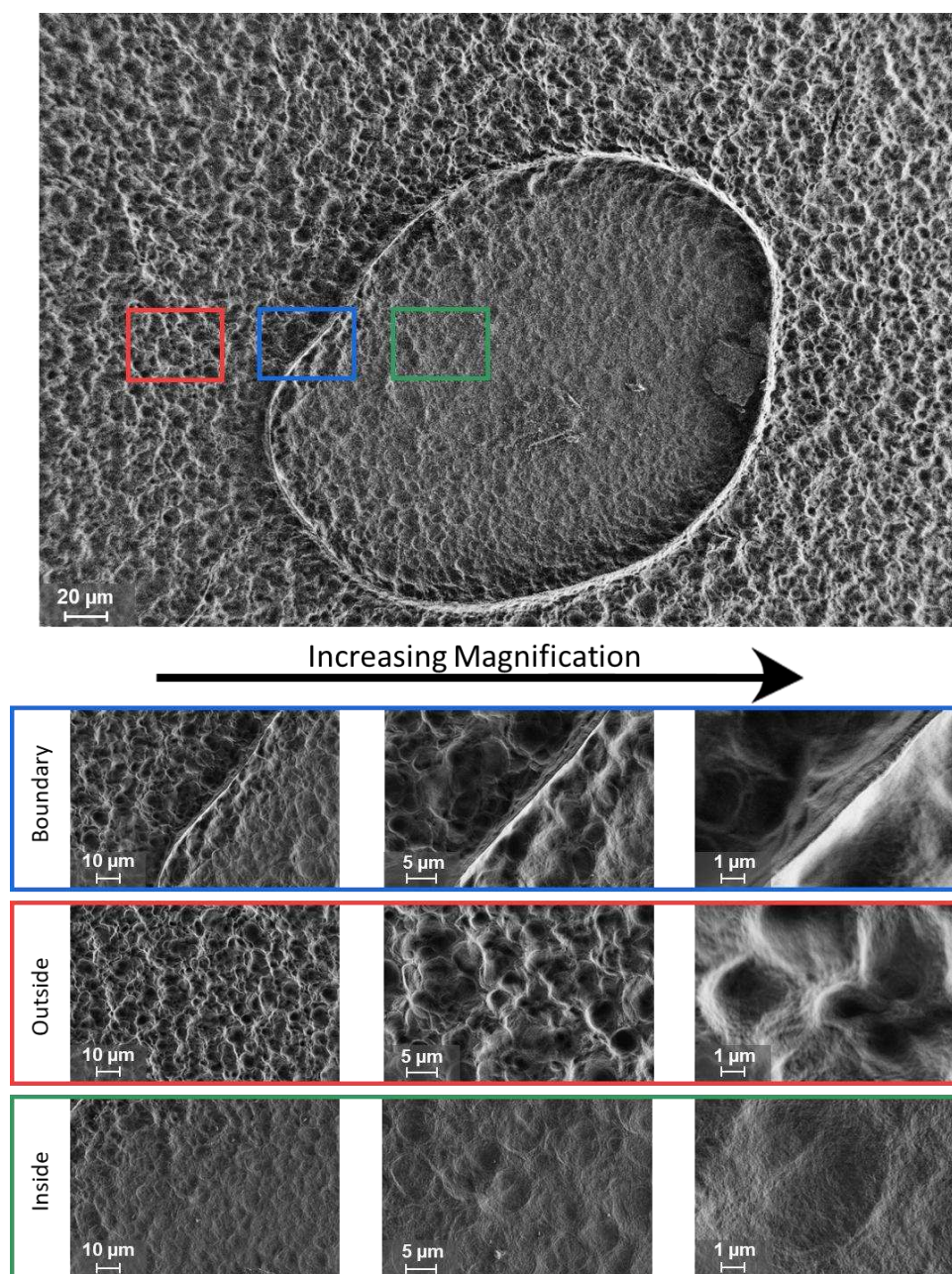


Figure S13. SEM image of a larger RUS phase condensate with images increasing in magnification for inside, outside and the boundary of the condensate. By looking at the boundary at high magnification, a difference in height between the inside and outside phases. The outside and inside phases show different morphology with inside showing a denser film-like morphology and the outside showing a more porous morphology.

Additional applications of RUS

Due to the excellent properties of the fibers spun from RUS, we decided to explore other potential applications. The most significant difference between RUS and traditional silk solutions is the development of phase condensates. Therefore, we explored applications that harness phase separation to either improve the properties or as a crucial mechanism in the production of the said application. One such application is microencapsulation. Phase condensates produced through complex coacervation have been used for microencapsulation for the last 100 years.^[12] During encapsulation, the coacervate envelops oil droplets stabilizing the droplets as a Pickering emulsion,^[13] which is then cross-linked to solidify the coacervate into a shell. However, these capsules require the use of cross-linkers such as glutaraldehyde, that compromise the biodegradability.^[14] By exploiting silk's shear sensitive nature, it was possible to induce encapsulation of the oil droplets without any cross-linkers in a one-pot synthesis (**Figure 8E** and **8F**). The lack of cross-linkers makes the capsules suitable for chemical-sensitive industries such as food, cosmetic, and pharmaceuticals. Additionally, the capsules maintained their cargo and did not collapse after drying, even at sizes as large as 200 μm . As drying makes the capsules brittle and easier to break, they are appropriately designed for burst release applications such as motion release deodorants and self-healing concretes.

We then moved on to comparing porous foams from RSF and RUS (**Figure 8A** to **8D**) Both foams initially appeared similar, with both having a porous structure with 10–20 μm voids. However, mechanical testing revealed that the RUS foams exhibited a yield stress 5 times and a stiffness over 3 times higher than RSF (**Table S3**). In fact, the 10 mm diameter foams were so stiff, they exceeded the maximum load of the 1 kN load cell. This demonstrates significant potential for use as a structural yet biodegradable material for bone tissue repair if the biocompatibility of the material can be established.^[15] While biomaterials produced from fibroin have been shown to have low immunogenic response,^[16] historical data suggested sericin causes immune response.^[17] Additionally, blends of the two proteins have been reported

to trigger immune response,^[18] which suggests RUS might be unsuitable for biomaterial applications. However, more recent studies have shown sericin to have excellent biocompatibility with an assortment of cell types.^[19] It is still unclear why blends of fibroin and sericin produce immune reaction,^[20] however these studies utilise degumming to remove sericin which is then re-added, leading to the contamination of degumming agents and degraded proteins that likely alter the immunogenic response. Therefore, biocompatibility assessment of RUS materials done in the future will not only enlighten the possibilities of future materials in this area but on the immunogenic response of mixtures of fibroin and sericin that have avoided degumming.

Table S3. Mechanical properties obtained from foam compression stress-strain curves (\pm SD).

Foam	Sample	Displacement [%]	Maximum Compressive stress [MPa]	Young's Modulus [MPa]	Yield stress [MPa]
RUS	1	30.4	18.5	77.2	3.7
	2	42.5	18.5	35.0	1.4
	Average	36.45 [\pm 8.6]	18.50 [\pm 0.0]	56.10 [\pm 29.8]	2.55 [\pm 1.6]
RSF	1	70.0	17.7	17.6	0.6
	2	70.0	19.6	16.2	0.4
	Average	70.00 [\pm 0.0]	18.65 [\pm 1.3]	16.90 [\pm 1.0]	0.50 [\pm 1.4]

Excel sheet S1. Raw data used to plot the Ashby diagram (Figure 2J) and their references. Most values were obtained through Koepfel *et al.* 2017 and Arakawa *et al.* 2022.^[7b, 21]

Video S1. RUS phase condensate coalescence. Phase condensates flow independently, occasionally merging into larger droplets.

Video S2. Influence of shear on RUS phase condensates. Phase condensates elongate into teardrop shapes with shear.

Video S3. RUS solution wet spun continuously into fibers through a 30% (wt/v) (NH₄)₂SO₃ bath. 30 meters of coagulated fiber was continuously collected on a roller at speed of 1 m min⁻¹ over a period of 30 minutes.

Supporting references

- [1] H.-J. Jin, D. L. Kaplan, *Nature* **2003**, 424, 1057.
- [2] a)B. J. Allardyce, R. Rajkhowa, R. J. Dilley, M. D. Atlas, J. Kaur, X. Wang, *Textile Research Journal* **2016**, 86, 275; b)Y. Yao, B. J. Allardyce, R. Rajkhowa, D. Hegh, A. Sutti, S. Subianto, S. Gupta, S. Rana, S. Greenhill, S. Venkatesh, X. Wang, J. M. Razal, *ACS Biomaterials Science & Engineering* **2020**, 6, 3197.
- [3] a)T. Saotome, H. Hayashi, R. Tanaka, A. Kinugasa, S. Uesugi, K.-i. Tatematsu, H. Sezutsu, N. Kuwabara, T. Asakura, *Journal of Materials Chemistry B* **2015**, 3, 7109; b)S. Inoue, K. Tanaka, F. Arisaka, S. Kimura, K. Ohtomo, S. Mizuno, *Journal of Biological Chemistry* **2000**, 275, 40517; c)P. R. Laity, E. Baldwin, C. Holland, *Macromolecular Bioscience* **2019**, 19, 1800188.
- [4] B. T. Kurien, R. H. Scofield, *Methods Mol Biol* **2012**, 869, 633.
- [5] T. Yoshioka, K. Tashiro, N. Ohta, *Biomacromolecules* **2016**, 17, 1437.
- [6] M. M. R. Khan, M. Tsukada, Y. Gotoh, H. Morikawa, G. Freddi, H. Shiozaki, *Bioresource Technology* **2010**, 101, 8439.

- [7] a)S. Chen, M. Liu, H. Huang, L. Cheng, H.-P. Zhao, *Materials & Design* 2019, 181, 108077; b)A. Koepfel, C. Holland, *ACS Biomaterials Science & Engineering* 2017, 3, 226.
- [8] T. Lefèvre, M. Auger, *International Materials Reviews* 2016, 61, 127.
- [9] a)P. Scherrer, *Nachrichten von der Gesellschaft der Wissenschaften zu Göttingen, Mathematisch-Physikalische Klasse* 1918, 2, 96; b)C. Guo, J. Zhang, X. Wang, A. T. Nguyen, X. Y. Liu, D. L. Kaplan, *Small* 2017, 13, 1702266.
- [10] a)R. Perret, W. Ruland, *Journal of Applied Crystallography* 1969, 2, 209; b)A. F. Thünemann, W. Ruland, *Macromolecules* 2000, 33, 1848.
- [11] P. Mohammadi, C. Jonkergouw, G. Beaune, P. Engelhardt, A. Kamada, J. V. I. Timonen, T. P. J. Knowles, M. Penttila, M. B. Linder, *Journal of Colloid and Interface Science* 2020, 560, 149.
- [12] D. W. Newton, B. C. Coacervates, B. A. Microencapsulation, B. A. Microencapsulation, C. A. Non-Microencapsulation, *Polymers for controlled drug delivery* 1991, 67.
- [13] S. Laquerbe, A. Carvalho, M. Schmutz, A. Poirier, N. Baccile, G. Ben Messaoud, *Journal of Colloid and Interface Science* 2021, 600, 23.
- [14] M. Zaki, Great Britain Patent WO2023285609.
- [15] T.-M. De Witte, L. E. Fratila-Apachitei, A. A. Zadpoor, N. A. Peppas, *Regenerative Biomaterials* 2018, 5, 197.
- [16] a)L. Meinel, D. L. Kaplan, *Advanced Drug Delivery Reviews* 2012, 64, 1111; b)J. Zhou, C. Cao, X. Ma, L. Hu, L. Chen, C. Wang, *Polymer Degradation and Stability* 2010, 95, 1679.
- [17] a)M. Dewair, X. Baur, K. Ziegler, *Journal of Allergy and Clinical Immunology* 1985, 76, 537; b)B. Panilaitis, G. H. Altman, J. Chen, H.-J. Jin, V. Karageorgiou, D. L. Kaplan, *Biomaterials* 2003, 24, 3079.
- [18] B. Ode Boni, B. Bakadia, A. Osi, Z. Shi, H. Chen, M. Gauthier, G. Yang, *Macromolecular bioscience* 2021, 22, e2100292.
- [19] a)Z. Wang, Y. Zhang, J. Zhang, L. Huang, J. Liu, Y. Li, G. Zhang, S. C. Kundu, L. Wang, *Scientific Reports* 2014, 4, 7064; b)P. Aramwit, S. Kanokpanont, W. De-Eknamkul, T. Srichana, *Journal of Bioscience and Bioengineering* 2009, 107, 556.
- [20] P. Aramwit, in *Silk Biomaterials for Tissue Engineering and Regenerative Medicine*, (Ed: S. C. Kundu), Woodhead Publishing, 2014.

- [21] K. Arakawa, N. Kono, A. D. Malay, A. Tateishi, N. Ifuku, H. Masunaga, R. Sato, K. Tsuchiya, R. Ohtoshi, D. Pedrazzoli, A. Shinohara, Y. Ito, H. Nakamura, A. Tanikawa, Y. Suzuki, T. Ichikawa, S. Fujita, M. Fujiwara, M. Tomita, S. J. Blamires, J.-A. Chuah, H. Craig, C. P. Foong, G. Greco, J. Guan, C. Holland, D. L. Kaplan, K. Sudesh, B. B. Mandal, Y. Norma-Rashid, N. A. Oktaviani, R. C. Preda, N. M. Pugno, R. Rajkhowa, X. Wang, K. Yazawa, Z. Zheng, K. Numata, *Science Advances* 2022, 8, eabo6043.